ELSEVIER

International Journal of Heat and Fluid Flow 23 (2002) 109–136

International Journal of HEAT AND FLUID FLOW

www.elsevier.com/locate/ijhff

Heat transfer research on gas turbine airfoils at NASA GRC

Vijay K. Garg *

AYT Research Corporation, NASA Glenn Research Center, Mail Stop 5-11, 21000 Brookpark Road, Cleveland, OH 44135, USA

Abstract

The turbine gas path is a very complex flow field due to a variety of flow and heat transfer phenomena encountered in turbine passages. This manuscript provides an overview of the current work in this field at the NASA Glenn Research Center (GRC). Based on the author's preference, however, more emphasis is on the computational work. There is much more experimental work in progress at GRC than that reported here. Specifically, the external flow and heat transfer characteristics are described over smooth and rough turbine blades for a range of parameter values. For smooth blades, the effect of film-cooling holes as well as internal cooling channels with ribs and bleed holes is considered. Studies on the blade tip region, susceptible to burnout and oxidation due to high thermal loading, are also described. Wherever possible, predictions of heat transfer coefficient on the real blade surface, obtained using in-house-developed codes, are compared with the available experimental data. Suggestions for further work are outlined.

Keywords: Gas turbine heat transfer; Film cooling; Internal cooling channel; Blade tip; Rough blade

1. Introduction

The turbine gas path is a very complex flow field. This is due to a variety of flow and heat transfer phenomena encountered in turbine passages. Stagnation flow heat transfer, heat transfer in the presence of steep pressure gradients both favorable and adverse, free stream turbulence, blade rotation and roughness (especially with use in the engine), unsteady blade/vane interactions, and three-dimensional effects such as tip leakage flow, the passage and horseshoe vortices are only some of the items in a long list of phenomena present in these passages. Fig. 1 illustrates some of these phenomena quite well.

Moreover, there is a growing tendency to use higher turbine inlet temperatures in order to improve the performance of a gas turbine engine. This implies increasing heat loads to the engine components. Modern gas turbine engines are designed to operate at inlet temperatures of 1800–2000 K, which are far beyond the allowable metal temperatures. Thus, to maintain acceptable life and safety standards, the structural elements need to be protected against the severe thermal environment. This calls for an efficient cooling system. The cooling technique currently used for high pressure turbines is a combination of internal and film cooling. In this technique, cooler air is injected into serpentine passages within the blade. Most of this air issues out of tiny (film-cooling) holes into the high temperature boundary layer on the blade surface, in an effort to form a cooler layer between the hot gas stream and the blade surface. Fig. 2 is a simplified illustration of the complex interactions between the internal and external flows.

The ultimate goal of the turbine designer is to maintain or increase the high level of turbine performance, and reduce, if possible, the amount of coolant flow needed to achieve this goal. Coolant flow, while necessary, is a penalty on the engine thermal efficiency. Accordingly, understanding the complex flow field and heat transfer associated with the coolant flow is a primary concern. It is important to understand both the film cooling and the internal coolant flow, particularly their combination.

Accurate prediction of turbine blade heat transfer, so crucial to the efficient design of blade cooling schemes, still remains a challenging task despite a lot of work in this area. The main cause for the lack of agreement with experimental data in such predictions is usually cited to be the turbulence modeling. As the direct numerical simulation of such flows is not anticipated to become

* Tel.: +1-216-433-6788; fax: +1-216-433-5802.
E-mail address: vijay.garg@grc.nasa.gov (V.K. Garg).

0142-727X/02/$ - see front matter
PII: S0142-727X(01)00144-8

Nomenclature

b	width of the cooling hole
c	true chord of the blade
C_f	skin friction coefficient
C_x	axial chord of the blade
d	hole diameter
D	hydraulic diameter; also leading edge diameter
Fr	Frossling number $(= Nu_D/\sqrt{Re_D})$
G	tip clearance height, expressed as percent of annulus height
h	heat transfer coefficient; also roughness height
h^+	wall normalized roughness height
k	turbulence kinetic energy
L	length of the hole-pipe
M	Mach number; also hole-row at the leading edge
Nu	Nusselt number
P	hole-row on the pressure side of the leading edge
q''	heat flux
Re	Reynolds number
Ro	rotation number $(= \Omega D/V)$
s	distance from the leading edge along the pressure or suction surface
S	hole-row on the suction side of the leading edge
St	Stanton number
T	temperature
Tu	turbulence intensity
v^*	shear velocity
V	characteristic velocity
x,y,z	Cartesian coordinate system with z in the spanwise direction
y^+	distance in wall coordinates $(= yv^*/v)$
z_n	$= (z - z$ for hub at trailing edge)/ blade span at trailing *edge*
ϵ	turbulence dissipation rate
η	film cooling effectiveness
v	kinematic viscosity
ρ	density
ω	specific turbulence dissipation rate $(= \epsilon/k)$
Ω	rotation rate of channel

Subscripts

2	value at exit
av	average value
c	for coolant
ex	value at exit
EQ	sand grain equivalent value
in	value at inlet
o	stagnation value or normalizing (base) value
rel	relative to rotor
w	value at wall

routine for many more years, turbulence modeling seems to remain the only option. By far the most popular turbulence models utilized today for flow and heat transfer calculations are the low-Reynolds number two-equation eddy viscosity models. The k–ϵ and k–ω are the most utilized models. These models offer a good balance between complexity and accuracy. The ability to mimic transition to turbulence which is often present on turbine blades and the ability to integrate to the walls are other reasons for their popularity. These models have been applied to a variety of experimentally measured cases and their accuracy assessed, yet they do not offer good comparisons consistently. There are also questions regarding the modeling of the stagnation heat transfer, and the free-stream turbulence intensity as well as the length scale.

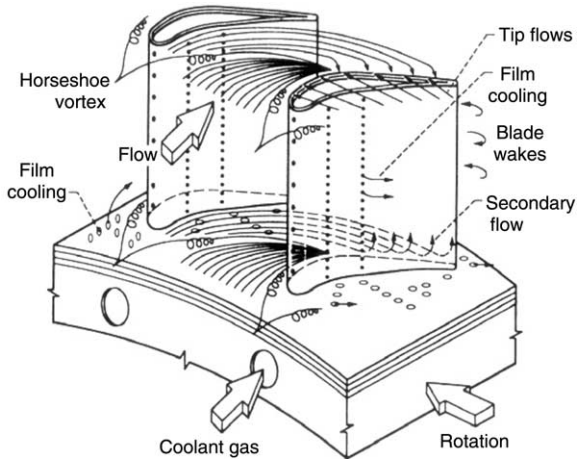

Fig. 1. Complex heat transfer phenomena in the turbine gas path.

Some well-documented data sets exist which test the capabilities of numerical schemes for the prediction of blade heat transfer. However, more data sets, especially on film-cooled turbine blades, are required for code validation. Most of the experimental data on film cooling have been confined to flat plates for a density ratio of unity. Only recently the use of liquid crystal techniques has started to yield surface, rather than discrete point, data. More such data are, however, required for improving the predictive capability.

This manuscript does not provide a comprehensive review of the vast literature in this field. Instead, it attempts to provide an overview of the current work in this field at the NASA Glenn Research Center. It builds on an excellent review by Simoneau and Simon (1993) on the understanding and prediction of heat transfer in the turbine gas path. Also, based on the author's pre-

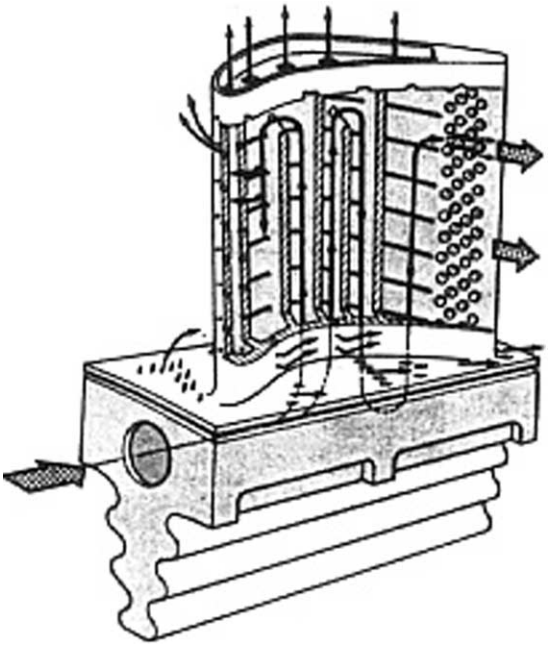

Fig. 2. A cooled turbine blade configuration, illustrating the complex interaction between internal and external flows.

ference, more emphasis is on the computational work. There is much more experimental work in progress at GRC than that reported here. For most computational work reported here, an in-house-developed code, currently called Glenn-HT, has been used. Some features of this code are detailed first. The rest of the manuscript describes the current work at GRC in four parts: external gas path with and without film cooling, including the blade tip region, the internal cooling channels with ribs and bleed holes within the turbine blade, and heat transfer on a rough blade.

2. The computational technique

Most of the numerical simulations described here have been performed using the NASA Glenn Research Center General Multi-Block Navier–Stokes Convective Heat Transfer code, Glenn-HT. Briefly, the code, formerly known as TRAF3D.MB (Steinthorsson et al., 1993, 1997), is an explicit, multigrid, cell-centered, finite volume code with a k–ω turbulence model without any wall functions. This is a general purpose flow solver designed for simulations of flows in complicated geometries. The code is based on the TRAF3D code, a single-block efficient code designed for simulations of gas turbine flows (Arnone et al., 1991, 1992; Arnone, 1994). The code employs the compressible Navier–Stokes equations in a rotating Cartesian coordinate system that is mapped onto a general body-fitted coordinate system using standard techniques. The multistage Runge–Kutta scheme developed by Jameson et al. (1981) is used to advance the flow solution in time from an initial approximation to the steady state. A spatially varying time step along with a CFL number of 4 is used to speed convergence to the steady state. Eigenvalue-scaled artificial dissipation and variable-coefficient implicit residual smoothing are used along with a full-multigrid method. Convective and diffusive fluxes are computed using central differences. The overall accuracy of the code is of second order. The TRAF3D code, modified for film cooling applications, was used by Garg and coworkers for some earlier film-cooling studies. The k–ω model of Wilcox (1994) with modifications by Menter (1993) and Chima (1996) has yielded good results for heat transfer on turbine blades, and is highly desirable for multi-block codes since it does not require the computation of distance from a wall. Also, no wall functions are used, thus avoiding any bias to the complex vortex structures near the blade and other surfaces.

While the Glenn-HT code has the original k–ω model (Wilcox, 1988), the shear stress transport (SST) model of Menter (1994), and the k–ω model of Wilcox (1998) were implemented in it by Garg and Ameri (2001) for comparing the experimental heat transfer data of Giel et al. (1999) on a transonic turbine rotor. The SST model encompasses both the k–ω and the k–ϵ models, with the original k–ω model of Wilcox (1988) activated in the near-wall region and the standard k–ϵ model (Jones and Launder, 1973) activated in the outer wake region and in free shear layers. Moreover, the definition of eddy viscosity is modified to account for the transport of the principal turbulent shear stress. An additional equation, a concentration equation, was added to the Glenn-HT code by Rigby (1998) to allow for the calculation of mass transfer under adiabatic conditions. The purpose of adding this additional convection–diffusion equation was to simulate naphthalene sublimation experiments which do not experience the effects of buoyancy that a heated rotating channel would experience. The concentration equation, of course, depends on the solution of the other equations, but has no effect on them.

2.1. Grid generation

All the structured multi-block grids described herein were generated using a commercially available package, GridPro™ (Program Development Corporation, 1997). This software generates full face matching blocks with a tendency to produce many small blocks. This is in general detrimental to computational efficiency. In order to merge the many elementary blocks into a minimum number of non-full face matching blocks, called super blocks, Rigby (1996) and Rigby et al. (1997b) developed the Method of Weakest Descent. This method has proven itself to be fast and very effective, and has since been included as part of the GridPro™ package. While the inviscid grid is first generated, the viscous grid is

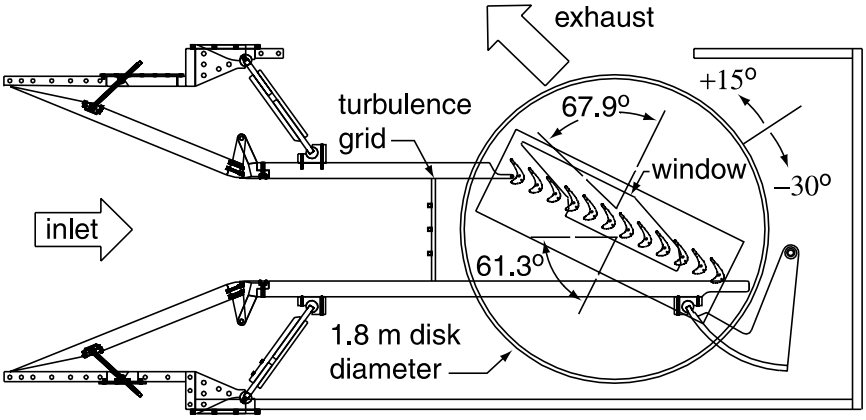

Fig. 3. Transonic turbine blade cascade (Giel et al., 1999).

obtained by clustering the inviscid grid near all the solid walls. The clustering is done in such a way as to ensure that in the viscous grid, the distance of any cell center adjacent to a solid wall, measured in wall units (y^+), is less than 1/2, following Boyle and Giel (1995). For computational accuracy, the ratio of two adjacent grid sizes in any direction is kept within 0.8–1.25. Any single-block grids have been generated using either the GRAPE code of Sorenson (1980) or the codes JERRY and TOM of Arnone (1992). Some general details on grid generation are available in Garg (1998a).

3. External gas path without film cooling

3.1. Experimental data on blade and endwall heat transfer

Detailed heat transfer measurements on the NASA Glenn transonic blade with 136° of turning and an axial chord of 127 mm are reported by Giel et al. (1999). Data were obtained for inlet Reynolds numbers of 0.5×10^6 and 1.0×10^6, for isentropic exit Mach numbers of 1.0 and 1.3, and for inlet turbulence intensities of 0.25% and 7.0%. Measurements were made in a linear cascade (cf. Fig. 3) having a highly three-dimensional flow field resulting from thick inlet boundary layers. Data were obtained by a steady-state technique using a heated, isothermal blade. Heat fluxes were determined from a calibrated resistance layer in conjunction with a surface temperature measured by calibrated liquid crystals. The purpose of the work was to provide benchmark quality data for three-dimensional CFD code and model verification. The experimental heat transfer measurements are available over the entire blade surface for varying exit Mach number, Reynolds number, inlet turbulence intensity as well as the inlet boundary layer thickness to the cascade. Some of the results on the unwrapped blade surface are shown in Fig. 4. These data depict highly three-dimensional behavior such as strong secondary vortical flows, laminar-to-turbulent transition, and shock impingement, thereby posing a severe challenge to the predictive ability of any numerical scheme. Data were also taken for endwall heat transfer in the same rig (Giel et al., 1998). One representative result is shown in Fig. 5 for $Re_{Cx} = 0.5 \times 10^6$, $M_{ex} = 1.3$ and $Tu_{in} = 7\%$. As required by most CFD analyses, the endwall heat transfer measurements show good periodicity. More experimental data on endwall heat transfer for Reynolds numbers between 73,000 and 495,000 are provided by Boyle and Russell (1990) using the liquid crystal technique.

Well-defined inlet flow measurements were provided by Giel et al. (1999) including those for the turbulence length scale, so important for CFD code validation, but often missing from experimental data. It is known (Garg and Ameri, 2001) that the turbulence length scale affects the passage vortex on the suction side of the blade – an essentially three-dimensional phenomenon. It is therefore essential to use a correct value for the turbulence length scale.

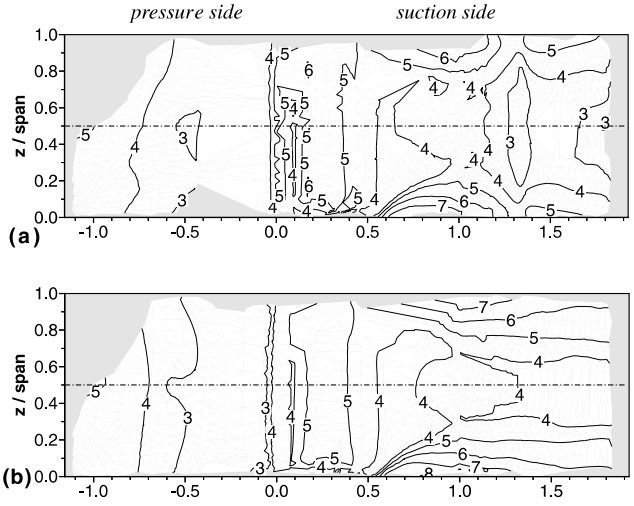

Fig. 4. Measured Stanton number × 1000 on the blade surface (Giel et al., 1999). (a) $Re_{in} = 10^6$, $M_{ex} = 1.32$, with grid; (b) $Re_{in} = 10^6$, $M_{ex} = 0.98$, with grid.

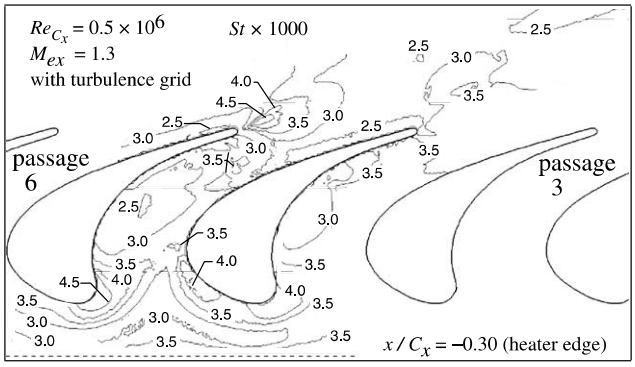

Fig. 5. Endwall Stanton number distribution (Giel et al., 1998).

3.2. Comparison with experimental data on a smooth blade

Giel et al. (1999) provide comparison of the experimental data with predictions using the three-dimensional Navier–Stokes analysis code, RVC3D, described by Chima and Yokota (1990) and by Chima (1991). A two-layer algebraic turbulence model, described by Chima et al. (1993), was used along with Mayle's model (Mayle, 1991) for initiation of transition. The transition length model of Boyle and Simon (1998), that includes Mach number effects, was used. Comparison between the experimental and computational results illustrated regions of good agreement and regions where modeling improvements are needed. Another comparison with this experimental data is presented by Garg and Ameri (2001). This prediction of the heat transfer on the blade surface was done using two versions of the k–ω model by Wilcox (1988, 1998), and the SST model by Menter (1994).

Fig. 6 shows the differences between the SST model and Wilcox (1998) k–ω model in terms of Stanton number distribution on the blade surface for $Re_{in} = 10^6$, $M_{ex} = 0.98$, with turbulence grid (Garg and Ameri, 2001). The experimental data for this case are shown in Fig. 4(b). The results in Fig. 6(a) provide a better comparison with the experimental data than those in Fig. 6(b). While the differences on the pressure surface and the leading edge are minor between the two models in Figs. 6(a) and (b), those on the suction surface are appreciable. The SST model yields a bigger passage vortex region near the hub, in better conformity with the experimental data, as compared to the k–ω model. This results in higher Stanton number values near the hub but slightly lower values near the mid-span on the suction surface of the blade for the SST model. This is clearly evident from Fig. 7 which provides a comparison with the experimental data at three spanwise locations (10%, 25% and 50%) on the blade for this case. While the computed Stanton number values based on either of the two models compare very well with the experimental

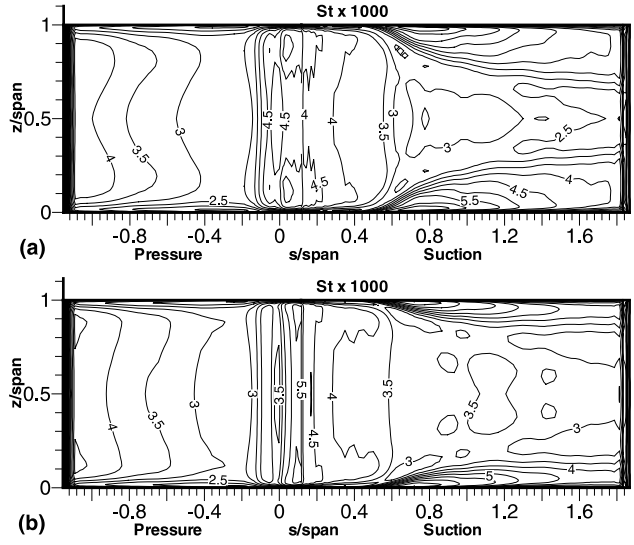

Fig. 6. Stanton number distribution on the blade for $Re_{in} = 10^6$, $M_{ex} = 0.98$, and turbulence grid using (a) SST model; (b) k–ω (1998) model (Garg and Ameri, 2001).

data on the pressure surface and the leading edge, there are discrepancies on the suction surface. The SST model yields a better comparison with the experimental data than the k–ω model at 10% and 25% spanwise locations, while the k–ω model yields a somewhat better comparison at mid-span. This appears to be a direct consequence of two phenomena: (1) a better resolution of the passage vortex region by the SST model, and (2) a better prediction by the k–ω model in large adverse pressure gradient regions. It may be noted that the largest adverse pressure gradient region lies near mid-span on the suction side of this rotor (Garg and Ameri, 2001), while at 10% spanwise location, there is almost no adverse pressure gradient region.

3.3. Stagnation-region heat transfer

Van Fossen et al. (1995) investigated experimentally the effects of freestream turbulence intensity, length scale, Reynolds number, and leading-edge velocity gradient on stagnation-region heat transfer. Heat transfer was measured in the stagnation region of four models with elliptical leading edges downstream of five turbulence-generating grids. Reynolds number, based on the leading edge diameter, ranged from 37,000 to 228,000, turbulence intensity ranged from 1.1% to 15.9%, and the ratio of integral length scale to leading-edge diameter ranged from 0.05 to 0.30. Stagnation-region heat transfer augmentation increased with decreasing length scale but an optimum scale was not found. A correlation was developed that fit heat transfer data for isotropic turbulence to within ±4% but did not predict data for anisotropic turbulence. The data of other researchers compared well with the correlation. Stagnation heat

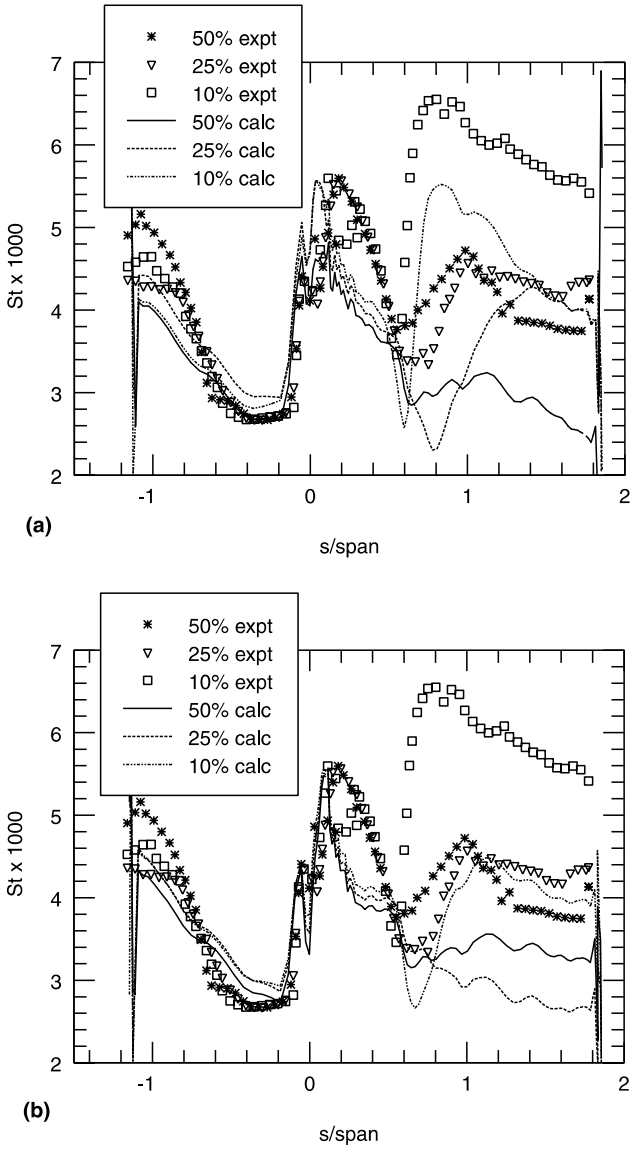

Fig. 7. Comparison with experimental data at three spanwise locations for $Re_{in} = 10^6$, $M_{ex} = 0.98$, and turbulence grid using (a) SST model; (b) k–ω (1998) model (Garg and Ameri, 2001).

transfer augmentation caused by turbulence was unaffected by the velocity gradient.

3.4. Numerical predictions

There have been several numerical predictions of heat transfer on a turbine blade. Some of these will be briefly described here. Boyle (1991) compared the numerical prediction of heat transfer with experimental data for seven turbine vane and blade geometries using a quasi-three-dimensional thin-layer Navier–Stokes analysis. Comparisons were made for cases with both separated and unseparated flows over a range of Reynolds numbers and freestream turbulence intensities. The analysis used the Baldwin–Lomax turbulence model modified to account for the effects of: (1) freestream turbulence on both transition and leading edge heat transfer; (2) strong favorable pressure gradients on relaminarizations; and (3) variable turbulent Prandtl number on heat transfer. Dunn et al. (1994) presented time-averaged heat transfer data on a two-stage turbine and compared with predictions obtained using a quasi-three-dimensional Navier–Stokes code. Boyle and Giel (1995) predicted heat transfer on turbine vanes and blades using a three-dimensional thin-layer Navier–Stokes code developed by Chima (1991), and compared with the available experimental data.

Ameri and Arnone (1996) studied the effect of transition modeling on the heat transfer predictions from rotating turbine blades using the code of Arnone (1994) with the Baldwin–Lomax turbulence model supplemented with Mayle's transition model (Mayle, 1991). The heat transfer predictions on the blade surface and hub endwall compared well with the experimental data of Blair (1991) taken in a low speed rig. On the blade surface, the prediction was found to improve with the inclusion of the transition-length model and wake-induced transition effects over the simple abrupt transition model. Boyle and Ameri (1997) described the effect of five different C-type grids on the predicted heat transfer and aerodynamic performance of a turbine stator. Predictions were obtained using a finite difference code and a finite volume code. The effect of different grids on blade heat transfer and overall performance was small. The most significant difference among the five grids occurred in the prediction of pitchwise variation in total pressure.

Boyle and Jackson (1997) compared the predictions of turbine vane and endwall heat transfer and pressure distributions with experimental data for two vane geometries at a Reynolds number of 5.3×10^6, a Mach number of 1.2, and a wall-to-gas temperature ratio of 0.66. Predictions were obtained by two different steady-state three-dimensional Navier–Stokes codes using algebraic turbulence models. Blade heat transfer predictions agreed reasonably well with the data on the pressure surface of either vane for all turbulence model assumptions. On the suction surface, however, there were differences. The location of transition on the suction surface using Mayle's model (Mayle, 1991) was bounded by the choice of local Tu used in the model. Assuming constant Tu resulted in early transition, and assuming the fluctuation constant resulted in transition too far aft on the vane suction surface. Differences in predicted endwall heat transfer among the different turbulence models were greater than the differences in experimental heat transfer between the two configurations. Both codes correctly predicted the spanwise variation in the wake behind the vane. However, both analyses predicted too low a value for the minimum

total pressure in the wake region, due perhaps to underprediction of pitchwise mixing.

A recent work by Boyle and Giel (2001) predicts turbine blade heat transfer in the presence of relaminarization. Accounting for the effects of relaminarization on blade heat transfer can substantially reduce the predicted heat transfer, leading in turn to reduced cooling requirements. Two-dimensional mid-span Navier–Stokes analyses were done for 18 test cases using 11 different turbulence models. It is shown that including relaminarization effects generally improves the agreement with experimental data.

3.5. Blade tip heat transfer

Turbine blade tips are susceptible to burnout and oxidation due to high thermal loading associated with flow through the tip clearance gap. This flow is caused by the pressure difference between the pressure and suction sides of the blade. The flow across the tip gap is also undesirable from the perspective of efficiency since it increases the losses in the flow. A detailed knowledge of heating patterns on and near the blade tip has been gained using predictive methods by Ameri and coworkers. Ameri et al. (1998) simulated the tip flow and heat transfer on the GE-E^3 first-stage turbine for a smooth tip, and with 2% and 3% recess. Two dominant flow structures were shown to exist within the recess. Also areas of large heat transfer rate were identified on the blade tip, and the mechanisms of heat transfer enhancement were discussed. No significant difference in adiabatic efficiency was observed for the three tip treatments investigated.

The heat transfer predictions on the blade tip (Ameri et al., 1998) are given in Fig. 8 along with the blade shape showing the tip recess and a part of the hub. Fig. 8(a) shows the Stanton number distribution on the flat tip. The patterns of heat transfer contours on the blade tip are similar to those in previous studies (Ameri and Steinthorsson, 1995, 1996). Figs. 8(b) and (c) show the Stanton number distribution on the rim and bottom of the cavity for the 2% and 3% recess, respectively. It is observed that the rate of heat transfer on the bottom of the cavity reaches higher values than those seen on the flat tip due to the flow impingement. On the rim of the squealer tip, the rate of heat transfer on the pressure side is comparable to that on the flat tip but is somewhat higher on the suction side. Fig. 9 shows the streamline patterns on the blade tip. At least two distinct vortices can be discerned to exist within the cavity. One vortex is

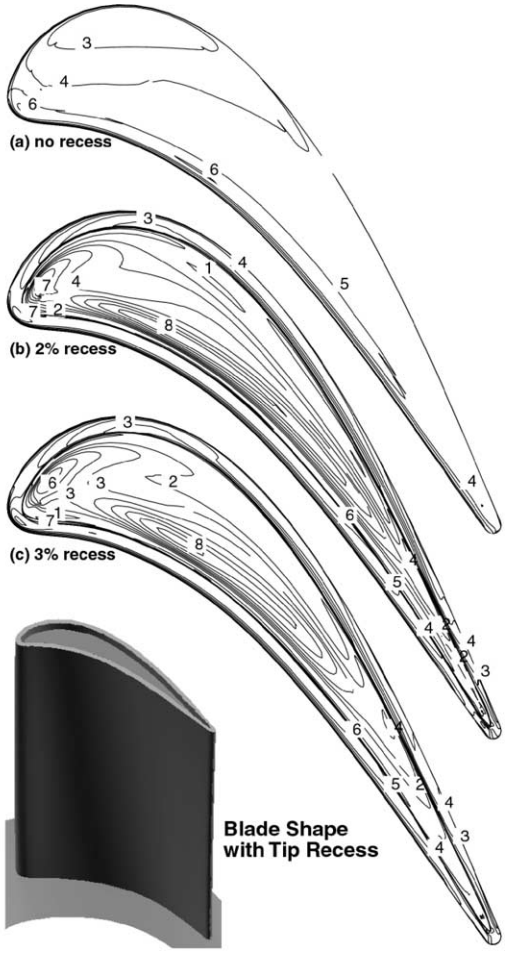

Fig. 8. Stanton number × 1000 on the cavity floor and rim for no recess, 2% and 3% tip recess (Ameri et al., 1998).

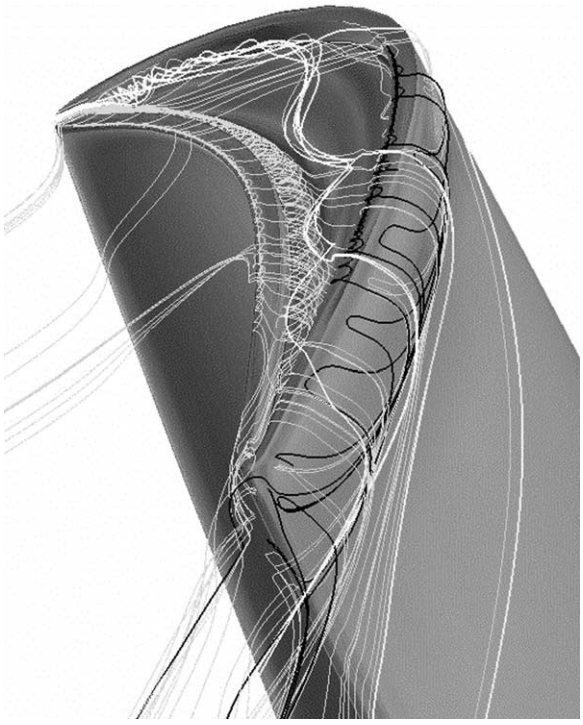

Fig. 9. Streamlines showing the blade tip flow patterns (Ameri et al., 1998).

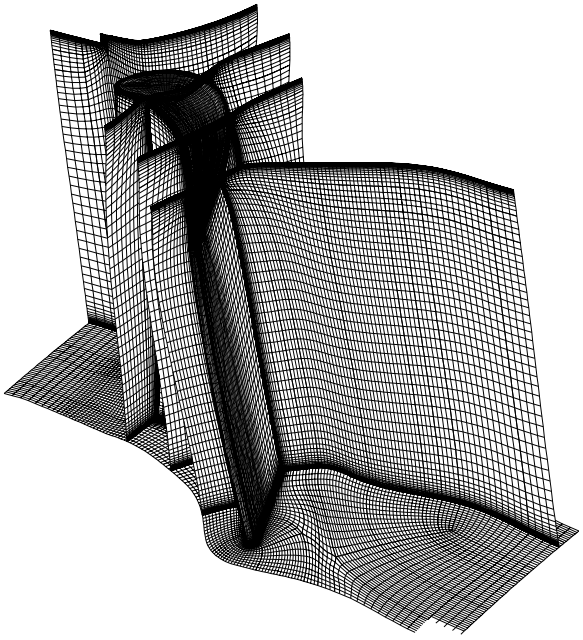

Fig. 10. Overall grid features for the GE-E^3 blade (Ameri et al., 1999).

a separation vortex, generated as the incoming flow separates off the inner edge of the pressure side rim. This vortex hugs the pressure side, sidewall and spills out of the cavity near the trailing edge of the blade. The second vortex, apparently a separation vortex as well, runs from the stagnation region to the suction side of the blade. These vortices are generated in addition to the separation vortex along the pressure side rim, suction side rim, and the blade suction side tip flow vortex.

Ameri et al. (1999) assessed the effect of tip leakage flow on the rate of heat transfer to the blade, blade tip, and casing. The effect on the exit angle and efficiency was also examined. Passage geometries with and without casing recess for the GE-E^3 first-stage turbine were considered. Clearance heights of 0%, 1%, 1.5% and 3% of the passage height were examined. For the two largest clearance heights considered, different recess depths were considered. There was an increase in the thermal load on all the surfaces due to enlargement of the clearance gap. Introduction of recessed casing resulted in a drop in the rate of heat transfer on the pressure side, but the picture on the suction side was found to be more complex for the smaller tip clearance. For the larger tip clearance, the effect of casing recess was an orderly reduction in the suction side heat transfer as the casing recess was increased. There was a marked reduction of heat load on the blade tip upon introduction of the casing recess; however, only a small reduction was observed on the casing itself. A linear relationship between the efficiency and tip clearance was confirmed. It was also observed that the casing recess has a small effect on the efficiency but can have a moderating effect on the flow under-turning at smaller tip clearances.

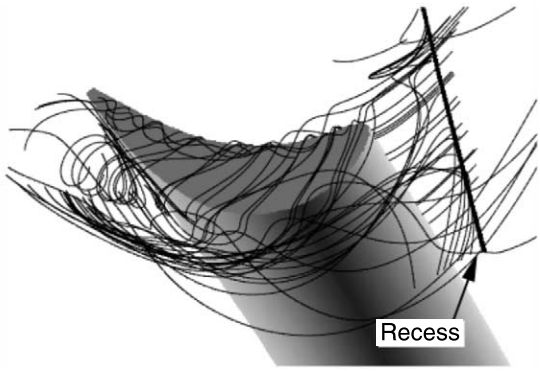

Fig. 11. Streamline patterns for 3% tip clearance and recess height, and 25% casing recess (Ameri et al., 1999).

Fig. 10 (Ameri et al., 1999) shows the blade geometry and basic features of the grid, generated using the commercial code GridPro™. The grid for the case with tip clearance and casing recess consists of 310 elementary blocks, which are merged into 29 super blocks using the Method of Weakest Descent (Rigby, 1996; Rigby et al., 1997b). The total number of grid points is around 1.3 million. Fig. 11 shows streamline patterns for a 3% clearance gap with a casing recess upstream. The edge vortex, suction side tip vortex, and a large structure that appears to be a horseshoe vortex are present. The low-momentum fluid behind the recess also appears to be joining this large structure. These structures enhance the heat transfer to the blade. Fig. 12 shows the Stanton number contours on the blade tip for three gap clearances. The line plot shows that the increasing tip clearance gap elevates the rate of heat transfer over the upstream part of the blade but has the opposite effect on the downstream part. Near the trailing edge, heat transfer is mostly dominated by the size and extent of the separation bubble.

Ameri and Bunker (2000) carried out numerical prediction of heat transfer on the first-stage blade tip of a large power generation gas turbine. A good comparison with experimental data was achieved through accurate modeling of the most important features of the blade passage and heating arrangement. A sharp edge and a radiused edge tip were considered. Results using the radiused edge tip agreed better with the experimental data, owing to the absence of edge separation on the tip of the radiused edge blade. The overall geometry and grid for the complete passage are shown in Fig. 13. The casing recess extended over the splitter plate as per the experiment. The grid consisted of 1.4 or 1.8 million cells depending on whether slip or no-slip side walls were used. Figs. 14 and 15 show the measured and computed heat transfer coefficients for the sharp edge and radiused edge tips. The largest relative difference between the experimental and predicted values for the sharp edge case is in the area of the "sweet spot" (Bunker et al.,

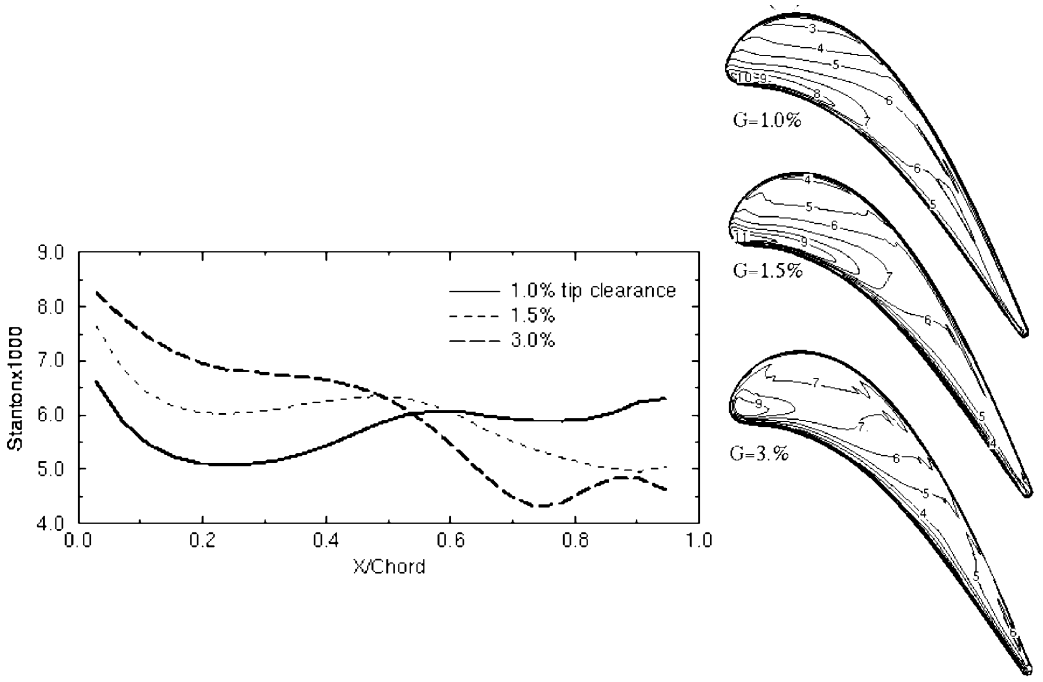

Fig. 12. With no recess (a) contours of Stanton number × 1000 over the blade tip for three gap widths, and (b) average tip heat transfer vs. the axial distance (Ameri et al., 1999).

2000) where the error reaches 30%. However, the agreement is good elsewhere and is generally below 15–20%. In addition, the region of high heat transfer rate in the trailing edge region, as observed experimentally, is correctly predicted. The agreement for the radiused edge tip (Fig. 15) is much improved over the sharp edge case, and is consistently better than 15% over the entire tip.

Ameri and Rigby (1999) predicted the distribution of heat transfer coefficient and cooling effectiveness on a blade tip with cooling holes. The computed effectiveness agreed quite well with the data of Kim and Metzger (1995), while agreement for the heat transfer coefficient was not as good but improved away from the cooling holes. Numerical flow visualization showed that the uniformity of wetting of the surface by the film-cooling

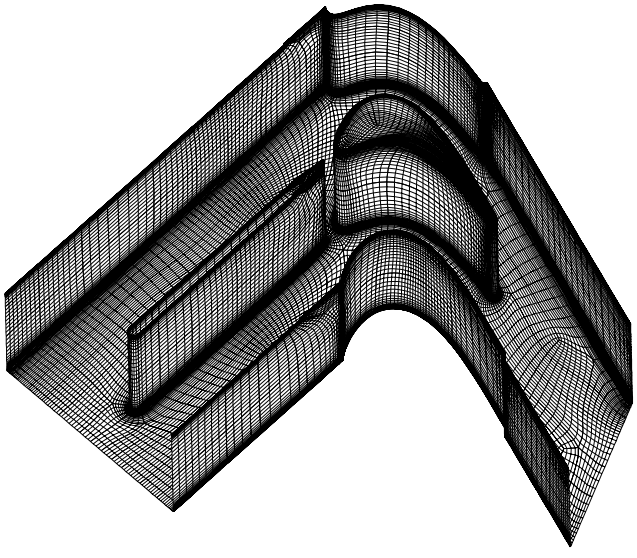

Fig. 13. Overall geometry and grid for the complete passage (Ameri and Bunker, 2000).

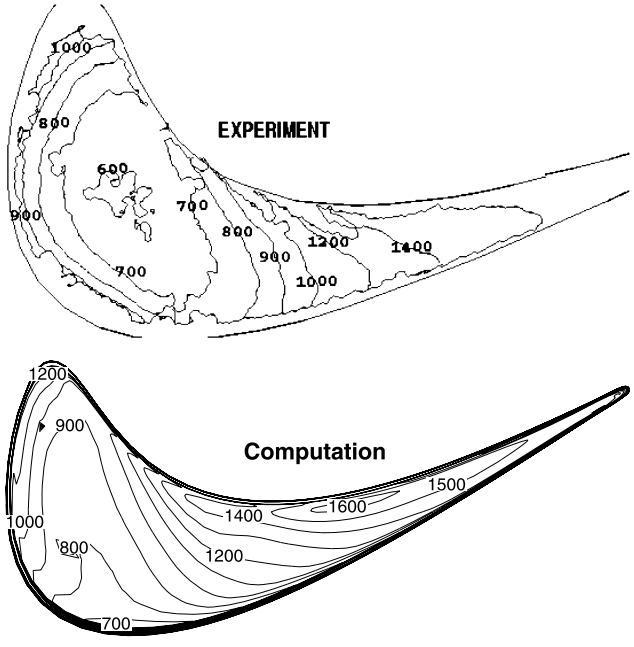

Fig. 14. Sharp edge tip heat transfer coefficient (W/m^2 K) for clearance of 2.03 mm and $Tu = 5\%$ (Ameri and Bunker, 2000).

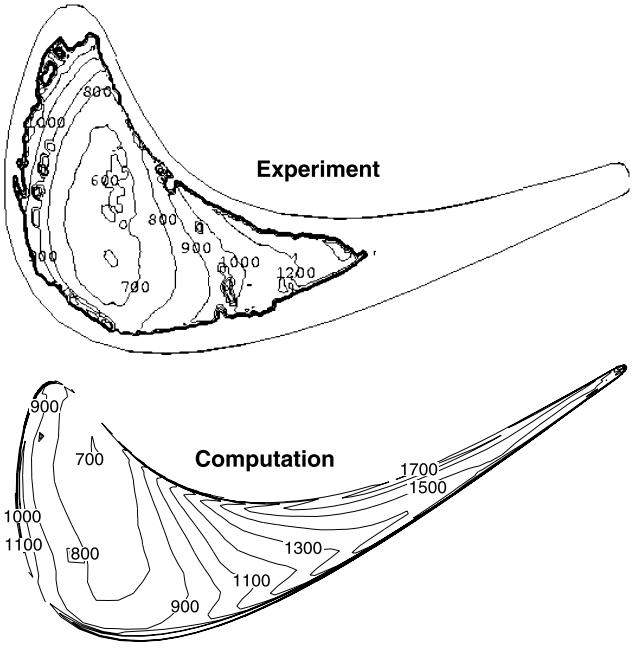

Fig. 15. Radiused edge tip heat transfer coefficient (W/m^2 K) for clearance of 2.03 mm and $Tu = 5\%$ (Ameri and Bunker, 2000).

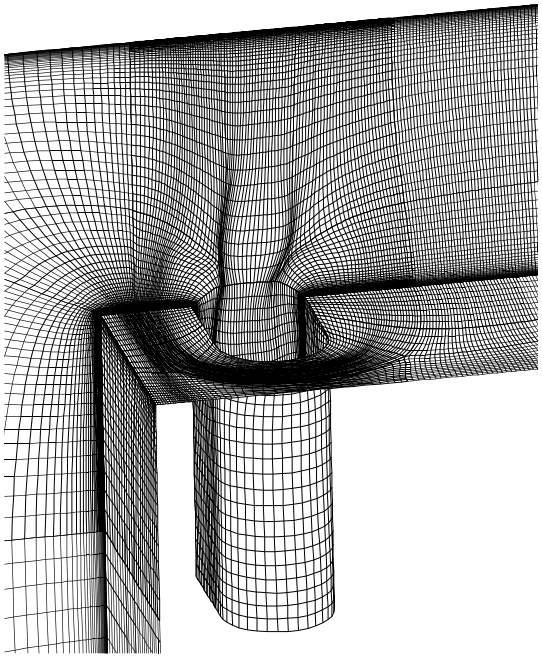

Fig. 17. Near-hole view of the grid (Ameri and Rigby, 1999).

jet is helped by the reverse flow due to edge separation of the main flow. While Fig. 16 shows the configuration that was tested by Kim and Metzger (1995) and gridded by Ameri and Rigby (1999), Fig. 17 shows details of the grid near the edge and injection hole. The spanwise symmetry between the holes and within the holes is used to minimize the size of the computational domain. Fig. 18 shows the flow near the hole. It is evident from Fig. 18 that the coolant air has covered the tip surface immediately downstream of the hole. Due to flow separation and backward flow of the mainstream, the fluid emerging out of the hole flows upstream and spills out the sides of the hole thus covering the surface between the holes. This helps the spanwise uniformity of h and η. Thus the proximity of the hole to the pressure side edge of the blade appears to be an important factor in tip film cooling. In Fig. 19 the distribution of η over the entire surface is shown where the relative uniformity is evident. Fig. 20 shows the comparison between the computed spanwise-averaged cooling effectiveness and the experimentally measured values. The overall agreement is quite good and improves with distance from the hole.

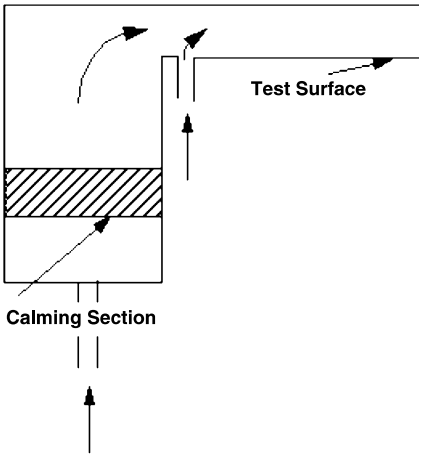

Fig. 16. Schematic of the tunnel tested and computed (Ameri and Rigby, 1999).

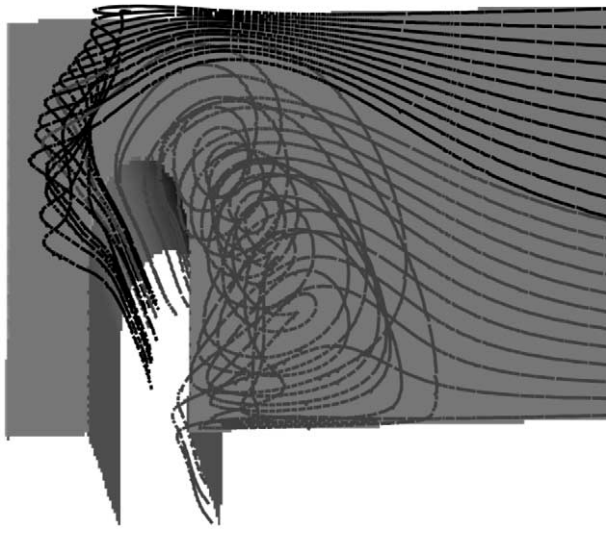

Fig. 18. Top view of the hole showing the coolant flow distribution on the surface (Ameri and Rigby, 1999).

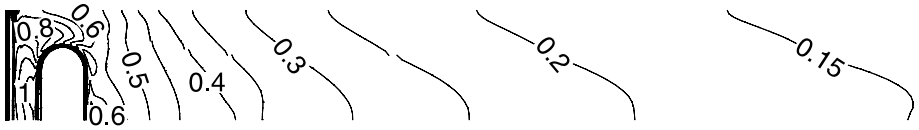

Fig. 19. Cooling effectiveness distribution over the surface (Ameri and Rigby, 1999).

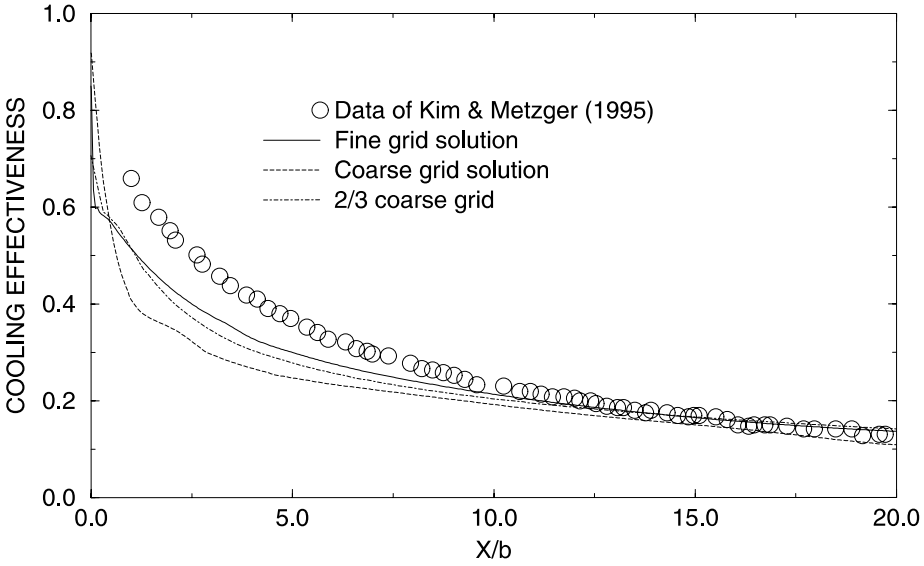

Fig. 20. Spanwise-averaged cooling effectiveness (Ameri and Rigby, 1999).

This figure also shows that the distribution resulting from two coarse grids is quite similar to that from the fine grid.

4. External gas path with film cooling

A considerable effort has been devoted to understanding the coolant film behavior and its interaction with the mainstream flow. The film cooling performance is influenced by the wall curvature, three-dimensional external flow structure, free-stream turbulence, compressibility, flow unsteadiness, the hole size, shape and location, and the angle of injection. Interest in this field has grown considerably in recent years. However, many studies on film cooling have been confined to simple geometries, for example, two-dimensional flat and curved plates in steady, incompressible flow.

An excellent survey of the film-cooling work up to 1971 has been provided by Goldstein (1971). Several further studies in this field have been summarized by Garg and Gaugler (1993, 1994, 1996). A number of parametric studies have been performed by Garg and coworkers to determine the effect of several parameters such as the effect of coolant velocity and temperature distributions at the hole exit (Garg and Gaugler, 1997a), the effect of blade rotation and of the direction of coolant ejection from the shower-head holes (Garg, 1997), the effect of spanwise pitch of shower-head holes (Garg and Gaugler, 1996), the effect of coolant to mainstream mass flow and temperature ratio (Garg and Gaugler, 1997b), and the effect of turbulence modeling (Garg and Abhari, 1997; Garg and Ameri, 1997; Garg, 1998b, 1999). Four turbulence models, the Baldwin–Lomax model, Coakley's q–ω model, Chien's k–ϵ model, and Wilcox's k–ω models, have been analyzed, and results compared with the experimental data for heat transfer from rotating as well as stationary blades. In all these studies by Garg and coworkers, coolant velocity and temperature distributions were prescribed at the hole exits. Moreover, while the true hole-exit on the blade surface is oval-shaped, it was approximated by a rectangle with steps owing to the use of a single-block grid. A recent study by Garg and Rigby (1999), using a multi-block grid, analyzed in detail the coolant flow structure issuing out of compound-angled shower-head holes on a real blade. The flow was resolved not just over the blade but also inside the three staggered rows of film-cooling hole-pipes and in the plenum where the cooling flow originates. This study also presented an extensive survey of the existing literature on the coolant flow characteristics at the exit of film-cooling holes. Heidmann et al. (2000) also analyzed in detail a film-cooled vane with 12 rows of holes, including six rows of shower-head holes and two rows of shaped holes. We will show some of their results later.

It is well known that a film-cooled blade has hundreds of holes out of which the coolant is ejected. In order to predict the heat transfer characteristics accurately on such a blade, it is intuitive to follow the coolant from the plenum into the hole-pipe and out of every hole-exit. However, for hundreds of holes on the blade, generation of a reasonable grid while tracing the coolant from the plenum to every hole-exit and beyond becomes extremely complex, if not impossible. The problem is much more tractable if the coolant flow characteristics could be specified at the hole exits on the blade, without going inside every hole. Even in such a case, grid generation is not trivial, and leads to at least a couple of million grid cells (Garg, 2000). There are two approaches to the solution of this problem. For one, Garg (2001) derived detailed coolant flow characteristics at the hole exits from an earlier analysis where the hole-pipes and coolant plenum were also discretized (Garg and Rigby, 1999), and tested them successfully on the same rotor. This revealed that very fine resolution of the grid normal to the hole-rim, as in the study by Garg and Rigby (1999), is not required for good prediction of the film cooling effect on the blade surface. The other approach, designed for a much coarser grid, is to model the film cooling effect in terms of source terms (Heidmann and Hunter, 2001). Let us look at a few salient results from some of these studies on film cooling.

4.1. Effect of coolant flow distributions at hole exits

Fig. 21 (taken from Garg and Gaugler, 1997a) shows the effect of coolant velocity and temperature distribution at the hole exit on the normalized heat transfer coefficient (solid and dash curves) at the C3X vane surface in comparison with experimental data (Hylton et al., 1988), denoted by □, for the case 44355 at a spanwise location (near mid-span) where the experimental data were taken. This vane has nine rows of film-cooling holes with five staggered rows of compound-angled holes on the shower head. The hole-exit distributions are detailed in Garg and Gaugler (1997a). The heat transfer coefficient values in this figure have been normalized with respect to an arbitrary value, $h_o = 1135.6$ W/m^2 K, as per Hylton et al. (1988). There are no data given for about 25% of surface length on either side of the leading edge since this portion contained the plenum chambers for injection of the colder gas and was insulated from the rest of the vane in the experimental tests. The fluctuations in the data are due to the non-uniform vane surface temperature in the experimental data. The nine short vertical lines near the center-bottom of this figure denote the location of film-cooling rows. The normalized heat transfer coefficient corresponding to the polynomial profiles of coolant velocity and temperature at the hole exit is about 50–60% higher than that corresponding to the 1/7th power law over most of the suction surface. However, the difference over the pressure surface is only about 35%. Also, the 1/7th power law profile results seem to match better with the experimental data than the polynomial profile results. More cases for the C3X vane and the VKI and ACE rotors are provided by Garg and Gaugler (1997a). They conclude that different velocity and temperature distributions of coolant at the hole exit can lead to as much as a 60% change in the heat transfer coefficient at the blade surface in some cases. Also, different effects are observed on the pressure and suction surfaces depending upon the blade as well as upon the hole shape, conical or cylindrical. Thus for an accurate prediction of the heat transfer coefficient, the simulation should include the region inside the cooling hole-pipes and the plenum within the airfoil.

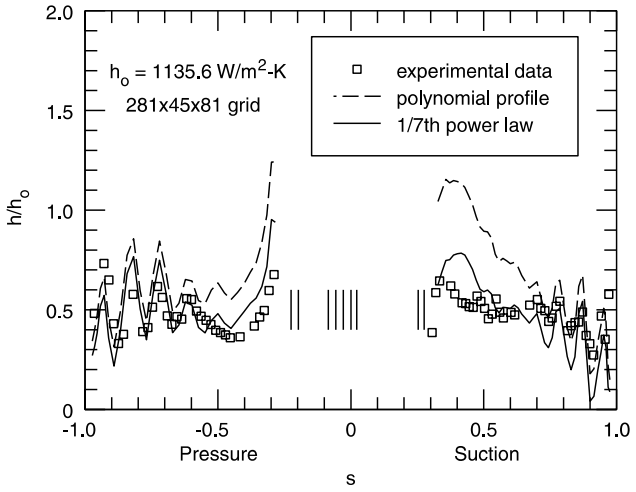

Fig. 21. Effect of coolant velocity and temperature profiles on the normalized heat transfer coefficient at the C3X vane surface for case 44355 (Garg and Gaugler, 1997a).

4.2. Coolant flow distributions determined at hole exits and resulting heat transfer

This call for a detailed analysis of the in-hole and near-hole physics was answered by Garg and Rigby (1999) and by Heidmann et al. (2000). Fig. 22 shows three staggered rows of cylindrical cooling holes ($d = 0.8$ mm) located around the leading edge of the VKI rotor tested by Camci and Arts (1985). These holes are spanwise angled at 30° from the tangential direction and drilled in a plane perpendicular to the blade surface. Details of the inviscid grid on the plenum, hole-pipes and the blade surface are also shown in Fig. 22. It can be observed that the grid quality is very good even near the sharp corners at the intersection of hole-pipes and blade or plenum. The grid, covering the inside of the plenum and hole-pipes for the coolant flow, and the outside of the blade for the main flow, was generated using the commercial code GridPro™. While the inviscid grid is

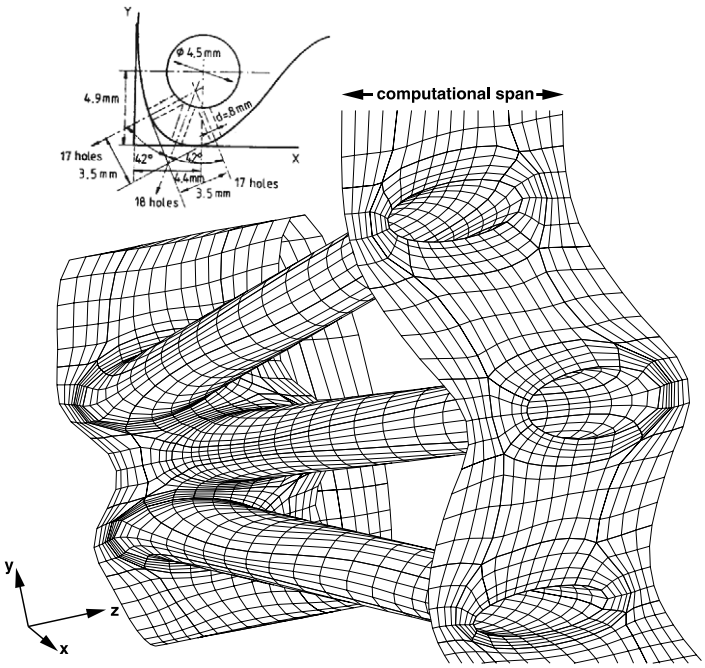

Fig. 22. Shower-head cooling holes and inviscid grid details on the plenum (left), the hole-pipes and the VKI blade surface (right) (Garg and Rigby, 1999).

shown here only for clarity, the flow solver is run on the *viscous* grid obtained by clustering the inviscid grid near all the solid walls, as detailed earlier. The viscous grid had 16,896 cells in each of the three hole-pipes, and 25,216 cells within the plenum.

Fig. 23 compares the span-averaged heat transfer coefficient on the cooled blade surface with the experimental data of Camci and Arts (1985), denoted by squares, for the case 155. The abscissa in this figure represents the surface distance along the blade normalized by the true chord, as per the experimental data of Camci and Arts (1985). The three short vertical lines at the bottom of this figure denote the location of shower-head cooling rows. Also shown is the blade heat transfer coefficient predicted by the analysis of Garg and Ameri (1997) using the k–ω model wherein, following Leylek and Zerkle (1994), 1/7th power-law distribution for the coolant velocity and temperature at the hole exits was specified, and the region inside the hole-pipes and plenum was *not* included in the computations. We may point out that Garg and Ameri (1997) compared the heat transfer coefficient on the VKI rotor corresponding to all six rows of cooling holes, not just the three rows of shower-head holes considered here. Thus for the dashed-line results in Fig. 23, the old code was specifically re-run. The superiority of the results, obtained by gridding inside the plenum and hole-pipes, is clearly evident on the suction surface of the blade, while on the pressure surface, both analyses yield an equally good comparison with the experimental data. As we will see, the coolant velocity and temperature distributions at any of the hole exits are different from the 1/7th power-law. It does appear, however, that there is negligible effect of coolant velocity and temperature distributions at the hole exit on the heat transfer coefficient on the blade pressure surface, but on the suction surface, the effect is considerable.

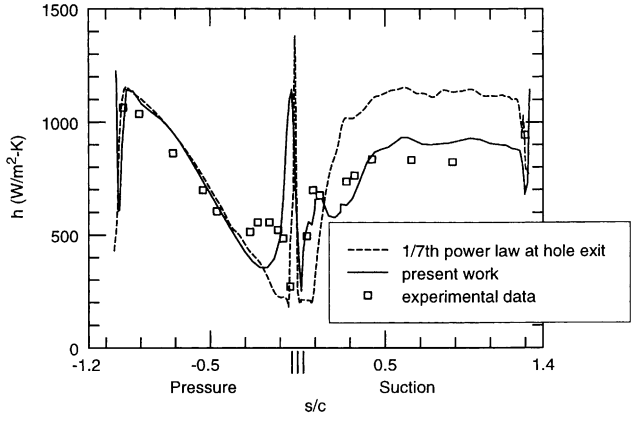

Fig. 23. Span-averaged heat transfer coefficient on the VKI blade surface for case 155 (Garg and Rigby, 1999).

Fig. 24 shows the normalized velocity, temperature, ρk and $\rho\omega$ contours at the shower-head hole-exits on the blade surface for the case 155. For the velocity contours, the magnitude of coolant velocity through the hole exit is normalized with respect to its average value over the hole exit, while for the temperature contours, the ratio, $(T_w - T)/(T_w - T_{av})$, is plotted, where T_{av} is the average temperature over the hole exit. The contours are shown

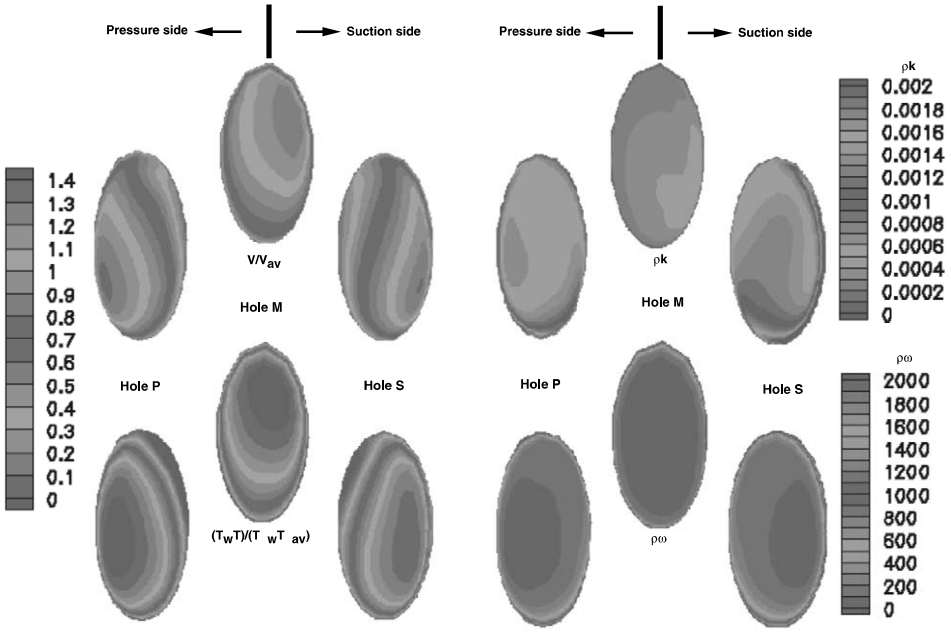

Fig. 24. Velocity, temperature, ρk and $\rho\omega$ contours at shower-head hole-exits on the VKI blade surface for case 155 (Garg and Rigby, 1999).

as if looking directly into the hole exit. From these contours, it is clear that the coolant flow at the exit plane of the leading edge hole, M, is deflected toward the suction side (due to the dynamic stagnation point located on the pressure side), and the coolant flow at the exit plane of the other two holes, P on the pressure side and S on the suction side, is deflected considerably in the direction of the main flow at these locations. Moreover, the velocity and temperature profiles at the exit plane of the holes do *not* follow the 1/7th power-law distribution that Leylek and Zerkle's analysis for a flat plate configuration (Leylek and Zerkle, 1994) would indicate for $L/d \geqslant 3.0$. For the VKI rotor $L/d \approx 6$ for the shower-head holes. The hole-exit plane profiles are more like higher-order polynomials, with considerable skewness for the P and S holes. It may be noted that 1/7th power-law profile yields a value of 1.224 for the ratio of maximum to average velocity, while here we have a value of about 1.3 for all holes. Similarly, for the temperature distribution, the 1/7th power-law would yield a maximum value of 1.2 for the ratio plotted, while we have a value of about 1.4 for all holes. The profiles for ρk and $\rho\omega$ are also skewed in the direction of the main flow over the holes P and S. However, $\rho\omega$ appears to be almost uniform over much of the hole-exit plane, except for the boundary layer effect near the hole-pipe wall.

Garg and Rigby (1999) also provided details of the highly complex vortex structure within a thin layer of thickness only about 2% of the hole diameter adjacent to the blade surface. Recalling that the hole diameter is only 0.8 mm, use of low-*Re* turbulence model is essential. For the fine grid normal to the blade surface, there were over eight grid cells within 2% of the hole diameter. Garg and Rigby (1999) also provided the distribution of coolant mass flow through each hole-pipe. The coolant mass flow is directly proportional to the pressure drop across the hole-pipe, being smallest through the hole M and largest through the hole S. Garg (2001) discretized the coolant flow characteristics at the hole exits found by Garg and Rigby (1999), and applied these to the shower-head hole-exits on the VKI rotor. A reasonably good comparison with the experimental data as well as with the more complete analysis of Garg and Rigby (1999), where the hole-pipes and coolant plenum were also gridded was obtained. Garg (2001) also found that for local values of the blade heat transfer coefficient, proper specification of the coolant flow characteristics at the hole exits is essential, and it is not really necessary to resolve the boundary layer along the hole-pipes as well as was done by Garg and Rigby (1999).

Heidmann et al. (2000) performed a realistic film-cooled turbine vane simulation using the Glenn-HT code. The simulation included the flow regions inside the coolant plena and film-cooling holes in addition to the external flow. The vane has two plena, which feed 12 rows of film-cooling holes as well as trailing-edge ejection slots, all of which were modeled by the grid. All rows have circular cross-sectional holes except for rows 1–4, which have shaped holes that are expanded in both the lateral and downstream directions. Rows 5–10 consist of compound-angled holes in the shower-head region with an inclination of 60° in the spanwise direction. Rows 11 and 12 have a spanwise pitch equal to two-thirds of the spanwise pitch of rows 1–10, so the com-

putational span for the vane covers three holes each in rows 11 and 12, and two holes each in rows 1–10. In rows 1–10, the holes are in a staggered arrangement, so it was necessary to split some holes on the spanwise periodic boundary. The commercial code GridPro™ was used to generate a multi-block grid for this complex geometry. The grid was initially composed of 1.2 million cells in 2298 blocks, which were merged to produce a grid consisting of 140 super blocks using the Method of Weakest Descent (Rigby, 1996; Rigby et al., 1997b). A blade-to-blade view of the multi-block grid is shown in Fig. 25, while details of the grid in the leading edge region of the vane are shown in Fig. 26. The faithful discretization of the shaped holes should be noted, as well as the ability of the multi-block grid to transition from a very fine structure near location of complex geometry such as film holes to a coarser structure far from the holes.

Fig. 27 shows the surface heat flux in the leading edge region of the vane. The spanwise variations are the largest on this portion of the vane. It should be noted that heat may flow from the fluid to the vane or vice versa because the wall temperature is between the free-stream and coolant temperatures. The largest heat flux occurs along the stagnation line, between rows 6 and 7, where the coolant is not present. Heat flux is also high in streaks between jets on the suction side portion of the shower-head region, and between the holes in the first row of shaped holes on the pressure side. This can be attributed to the twists and turns in the coolant streamlines shown in Fig. 28, where the vane surface is colored by the heat flux. Heidmann et al. (2000) also provide details of the complex distribution of coolant characteristics at the hole exits, as well as the film cooling effectiveness on the vane surface. The analyzed vane is the subject of an upcoming NASA Glenn Research Center experiment that will provide a real blind test for the numerical simulation.

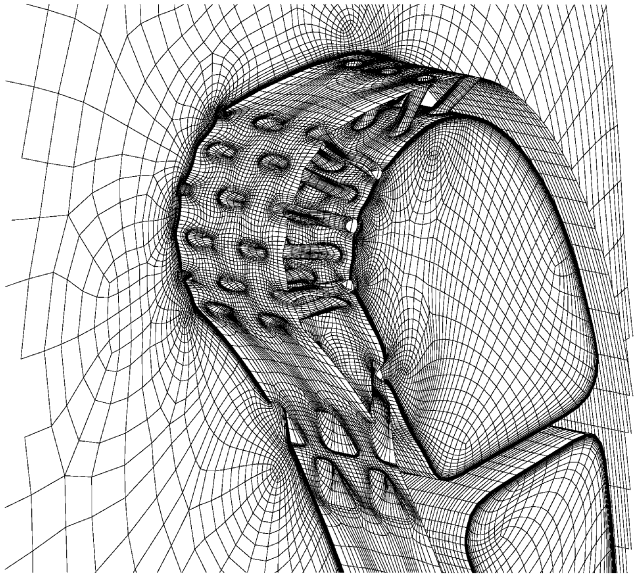

Fig. 26. Leading edge region of the computational grid (Heidmann et al., 2000).

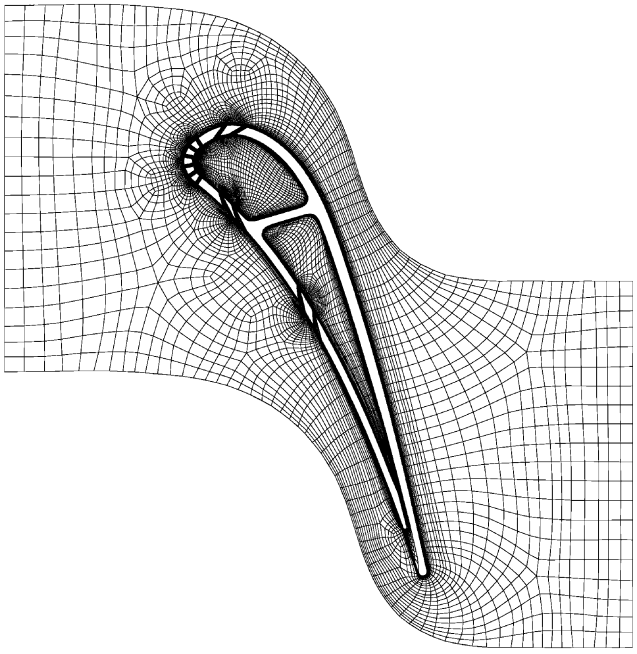

Fig. 25. Blade-to-blade view of multi-block grid (Heidmann et al., 2000).

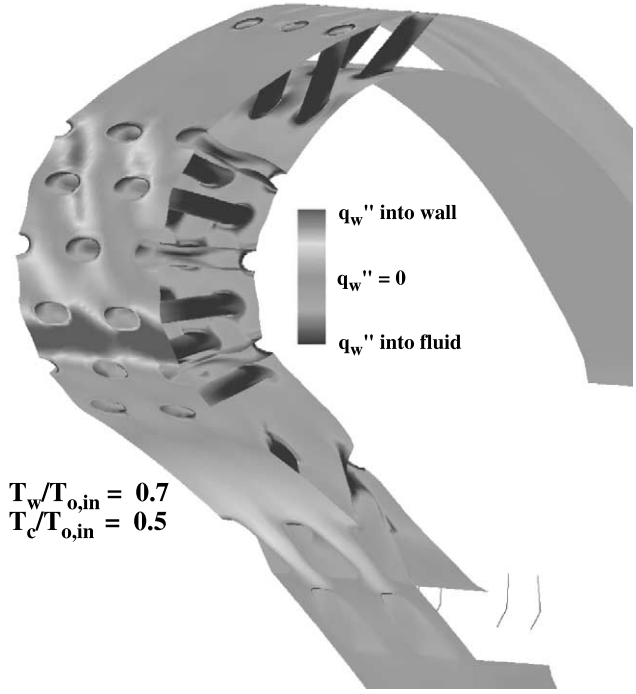

Fig. 27. Heat flux in the leading edge region on the vane surface (Heidmann et al., 2000).

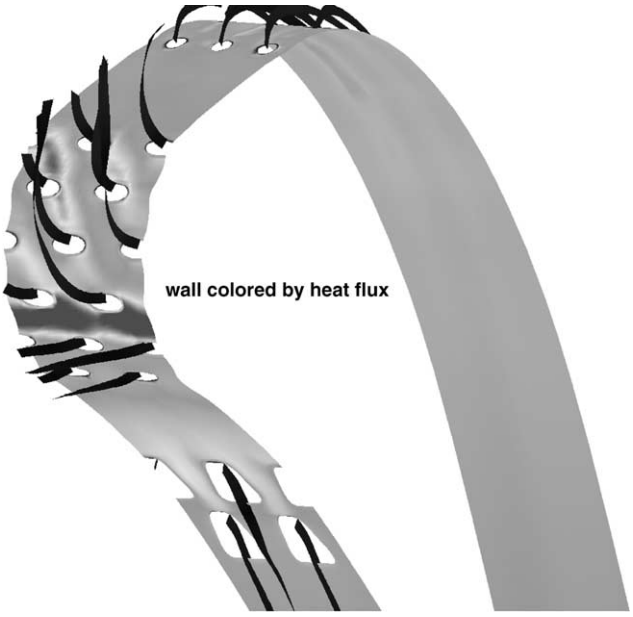

Fig. 28. Coolant streamlines out of hole exits (Heidmann et al., 2000).

4.3. The real film-cooled rotor

While studies by Garg and Rigby (1999) and by Heidmann et al. (2000) are essential to understand the coolant flow characteristics at the hole exits on an actual blade, they cannot be applied to a rotating blade since one has to consider all the holes, which may be a few hundreds, on the blade. For a non-rotating blade such as those analyzed by Garg and Rigby (1999) and by Heidmann et al. (2000), only one or two spanwise pitches of the holes are enough for numerical simulation, thus limiting the number of hole-pipes for analysis. For a rotating blade, the computational domain consists of the entire blade (with hundreds of holes), the hub and the shroud along with the tip clearance region. In such a case, it is still very difficult to generate a grid that extends into all the cooling hole-pipes and plena. For a rotating high pressure turbine blade with 172 film-cooling holes in eight rows, Garg (2000) specified polynomial distribution of coolant velocity (relative to the blade) and temperature at the hole exits. All the 172 holes were cylindrical with a diameter of 0.381 mm. Three rows (3, 4 and 5) were staggered with compound-angled holes on the shower head. In order to study the effect of gridding the tip clearance gap versus use of a tip clearance model, two grids were generated, one with the tip clearance gap gridded and the other without. Fig. 29 shows the multi-block grid on the blade tip and pressure side, and a part of the hub.

Initially, the entire grid, including that on the blade tip, consists of 4818 elementary blocks, but before the solver is used, it is merged into 280 super blocks using the Method of Weakest Descent (Rigby, 1996; Rigby et al., 1997b). For so many superblocks, generation of the connectivity file and the data file for the application of boundary conditions was automated. There were a total of 1016 boundary condition patches on the blade surface, of which 516 were over the 172 hole exits and the remaining 500 on the blade solid surface including the tip. An additional 15 boundary condition patches covered the hub, the shroud, and inlet and exit for the main flow. In the above details, periodic boundary condition patches are not accounted for since the code takes care of periodicity via the connectivity data for the blocks. The final viscous grid for the film-cooled blade consists of a total of 1,987,520 cells, with 80 cells in each of the 172 hole exits. For the uncooled blade, the grid consists of only 1,119,040 cells; the difference of 868,480 cells accounts for the presence of 172 film-cooling holes on the cooled blade. This amounts to an increase of about 5050 cells per hole for the cooled blade grid. If one could grid inside each of the 172 hole-pipes and the plena supplying the coolant to the holes, the increase in the grid size would be quite significant. Computations were performed in multi-processor mode on the 16-processor C90 or J90 supercomputer at NASA Ames Research Center. The code requires about 275 million words of core storage with all blocks in the core memory, and another 40 million words of scratch disk space. It takes about 90 s per iteration at the finest grid level. A case requires about 1500 iterations to converge.

Results were obtained for the heat transfer coefficient at the blade (rotating at 11,570 rpm) including the tip,

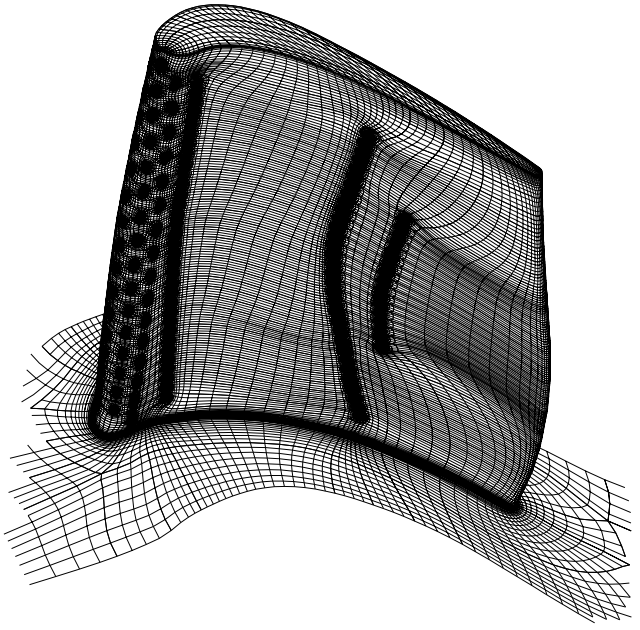

Fig. 29. Grid on the blade tip and pressure side, and a part of the hub (Garg, 2000).

hub and shroud surfaces for isothermal walls, and also for film cooling effectiveness on an adiabatic blade. For the cooled isothermal or adiabatic blade, two orientations of the shower-head hole rows 3, 4 and 5 were analyzed; one called "case 1" refers to coolant ejection from the shower-head holes towards the hub, and another called "case 2" refers to this ejection towards the blade tip.

Fig. 30 compares the heat transfer coefficient on the uncooled blade surface with that on the cooled blade surface for both orientations of the shower-head holes when there is a grid in the tip clearance gap. These distributions are represented on the s–z_n plane, where s is the surface distance along the pressure or suction surface measured from the leading edge, and z_n is the z-coordinate measured from that for hub at the blade trailing edge, both normalized by the span at the trailing edge of the blade. We note that the heat transfer coefficient is high in the leading edge region between the hub and blade mid-span, and all along the tip of the blade (even on the cooled blade). It is also high on the suction surface near the tip just downstream of the leading edge. This is due to the flow crossing over from the pressure to the suction side through the tip clearance gap. High values of h in the leading edge region of the cooled blade are due to a rather low amount of coolant injected through the shower-head rows of holes. In fact, the portion of the blade leading edge between the hub and blade mid-span is not covered by the coolant at all, as is evident from the streamlines shown and discussed later in Fig. 33. The heat transfer coefficient on the cooled blade surface is generally lower, especially on the pressure surface, than that on the uncooled blade. While h varies considerably in both the streamwise and spanwise directions on the suction surface, its spanwise variation is weaker than the streamwise variation on the pressure surface except in the boundary layers near the hub and tip. For the uncooled blade, the heat transfer coefficient is almost uniform over a large part of the pressure surface. For the cooled blade, there is little difference between the h distributions for the two orientations of shower-head holes.

Fig. 31 shows the film cooling effectiveness distribution on the adiabatic blade surface represented by s–z_n coordinates for both orientations of the shower-head holes when there is a grid in the tip clearance gap. The effectiveness is the lowest in the leading edge region and near the tip, especially over the suction surface. Since h and η are both based on the difference from $T_{o,rel}$, it is natural to expect low values of η where h is high, and vice versa (cf. Fig. 30). Fig. 32 shows the details of film cooling effectiveness in the leading edge region near rows 2 through 6 for both orientations of the shower-head holes, again with a grid in the tip clearance gap. The low

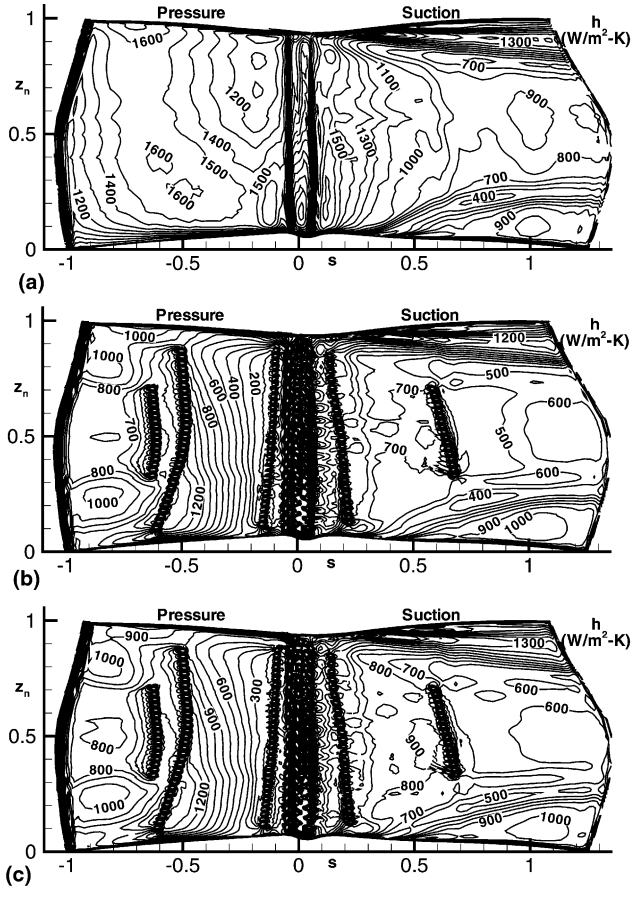

Fig. 30. Heat transfer coefficient on the blade surface with grid in the tip clearance gap (Garg, 2000). (a) Uncooled blade; (b) cooled blade (case 1); (c) cooled blade (case 2).

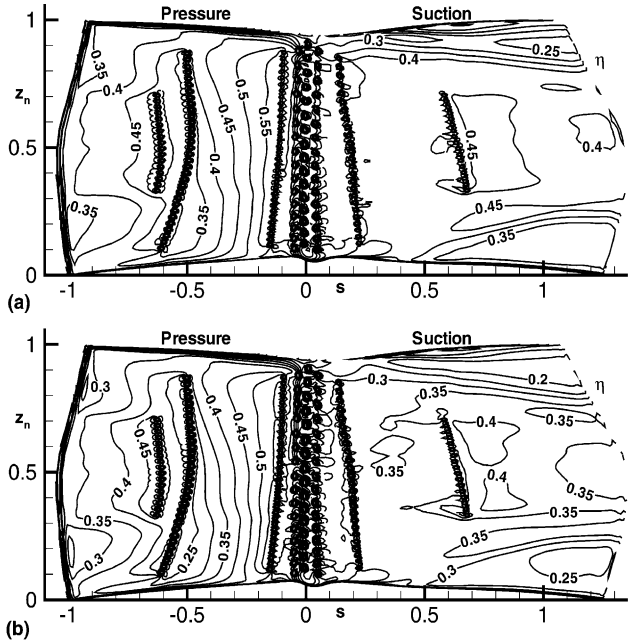

Fig. 31. Film cooling effectiveness on the adiabatic blade surface with grid in the tip clearance gap (Garg, 2000). (a) Case 1; (b) case 2.

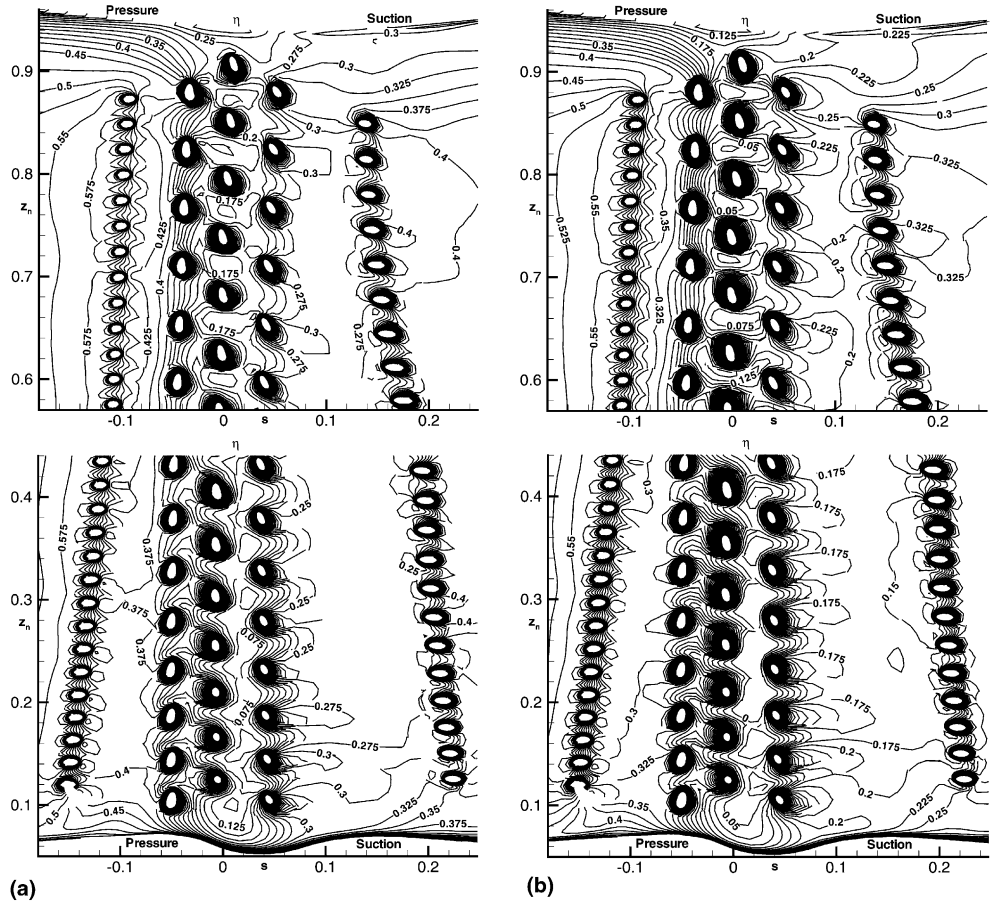

Fig. 32. Film cooling effectiveness in the leading edge region on the adiabatic blade surface with grid in the tip clearance gap (Garg, 2000). (a) Case 1; (b) case 2.

effectiveness regions over the blade leading edge are clearly visible.

Fig. 33 shows the streamlines, colored by stagnation temperature, emanating from holes over the cooled blade surface for case 1 with grid on the blade tip. While the complex vortical structure is clearly visible on the suction side near the blade tip (Fig. 33(a)), more interesting is the split of coolant flow from the leading edge hole row 4 in Fig. 33(b). A close look at Fig. 33(b) reveals that the coolant from the lower eight holes in row 4 flows towards the pressure side, while that from the upper eight holes flows towards the suction side. Thus, the stagnation line for the mainstream flow is between rows 4 and 5 from hub to blade mid-span, and between rows 3 and 4 from mid-span to blade tip. Due to this, there is no coolant over the leading edge region of the blade from hub to mid-span between rows 4 and 5. This leads to the high heat transfer coefficient or the low effectiveness values in this part of the blade. Also clear from Fig. 33(b) is that some of the coolant from holes near the hub in rows 2 and 3 flows towards the hub. This leads to a reduction in the heat transfer coefficient on the part of hub near the pressure side of the cooled blade.

Fig. 34 shows the streamlines, colored by stagnation temperature, approaching the cooled blade near the hub and several sections of the span for case 1 with grid on the blade tip. Fig. 34(a) shows the passage vortex flow clearly on the suction side of the blade while Fig. 34(b) shows evidence of the horseshoe vortex. Fig. 34(d) shows that the mainstream approaching the blade between the hub and mid-span splits at the leading edge such that the part over the pressure surface covers almost the entire pressure side from hub to tip. Also, a part of the mainstream between mid-span and blade tip crosses over to the suction side through the tip clearance gap while the rest remains on the pressure side, unmixed with the coolant. Fig. 34(c) reveals the contribution of various streams along the blade span to the vortical structures on the suction side of the blade.

Garg (2000) found that the heat transfer coefficient is much higher on the blade tip and shroud as compared to that on the hub for both the cooled and the uncooled cases, due to the flow through the tip clearance gap. The effect of gridding the tip clearance gap versus use of a tip clearance model is found to be small as far as the heat transfer coefficient or the adiabatic film cooling effec-

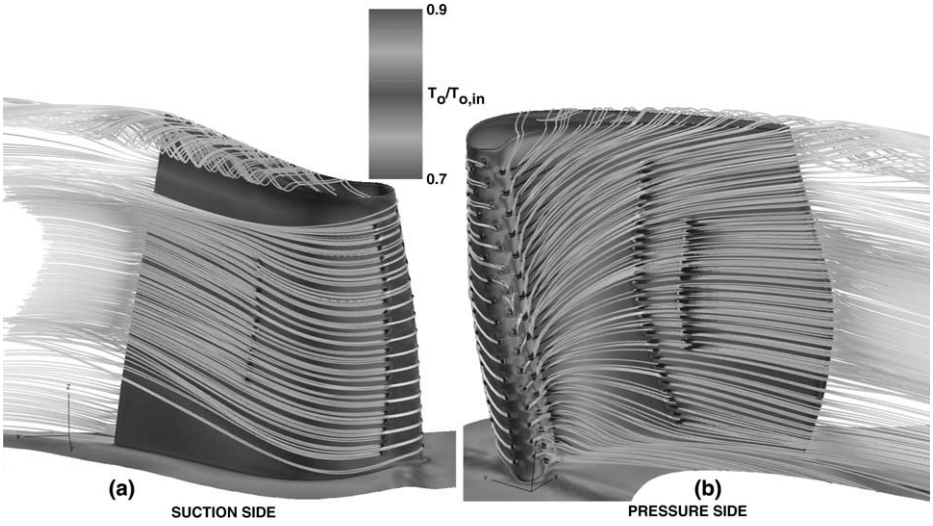

Fig. 33. Streamlines, colored by temperature, emanating from holes over the cooled blade surface with distribution of h (Case 1; grid on blade tip) (Garg, 2000).

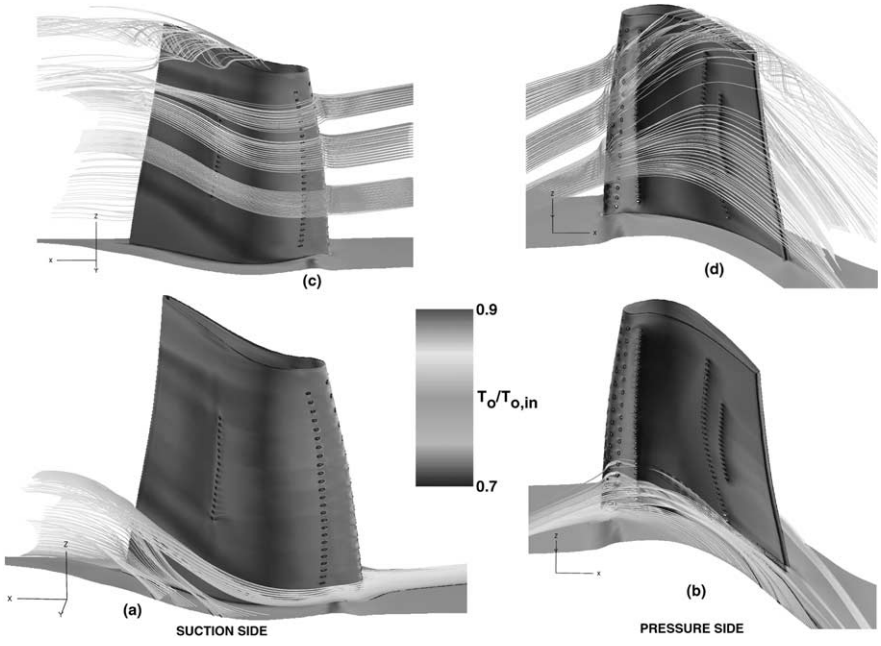

Fig. 34. Streamlines, colored by temperature, over the cooled blade surface with distribution of h (Case 1; grid on blade tip) (Garg, 2000).

tiveness on the blade surface is concerned. However, for heat transfer from the blade tip and the shroud, the tip clearance gap must be gridded. Use of a tip clearance model not only yields unrealistic values of heat transfer coefficient on the shroud, it cannot provide these values on the blade tip at all. The effect of different orientations of coolant ejection from shower-head holes is found to be small for heat transfer from the blade (including the tip), hub and shroud. This blade is the subject of an upcoming experiment at the Ohio State University that will provide a real blind test for the numerical simulation.

5. Internal channel flow

In addition to film cooling described above, there are complicated internal cooling passages within the turbine blade through which the cool air bled from the compressor flows through before exiting via the film-cooling holes. A lot of experimental and computational work has been carried out to analyze the heat transfer to/from these passages. Rigby et al. (1996) simulated the three-dimensional flow and heat transfer in a rectangular duct with a 180° bend. Results were presented for Reynolds numbers, based on the hydraulic diameter, of 17,000

and 37,000, and for aspect ratios of 0.5 and 1.0. A direct comparison between single-block and multi-block grid simulations was made. The multi-block grid system was found to yield more accurate results than the single-block grid with the same number of cells. Fig. 35 shows the contours of Nusselt number, normalized by the value for fully developed turbulent pipe flow, for the 0.5 aspect ratio duct and $Re = 17,000$ for the finest single-block grid, the multi-block grid and the experimental data of Arts et al. (1992). While both the single-block and multi-block grids produce the two peaks in heat transfer, the peak values predicted by the multi-block grid match the experimental data more closely. Moreover, the shape of the contours entering the first corner is better predicted by the multi-block solution with only one-third the number of cells. None of the predictions, however, produces the elevated heat transfer which the experimental data reveal near the inner wall, downstream of the bend, where the primary separated flow reattaches. Reasons for this deficiency in the computed solution may be a lack of streamwise resolution at the reattachment point and/or a weakness in the k–ω turbulence model. Fig. 36 shows the normalized Nu contours on the outer wall of the return channel for the same conditions as in Fig. 35. As expected, a peak in the heat transfer is observed a short distance from the corner, where the high-momentum fluid in the center of the duct impinges on the side wall. The location of the peak obtained with the multi-block grid matches the experimental data well, whereas with the single-block grid, the peak location is too far downstream of the corner.

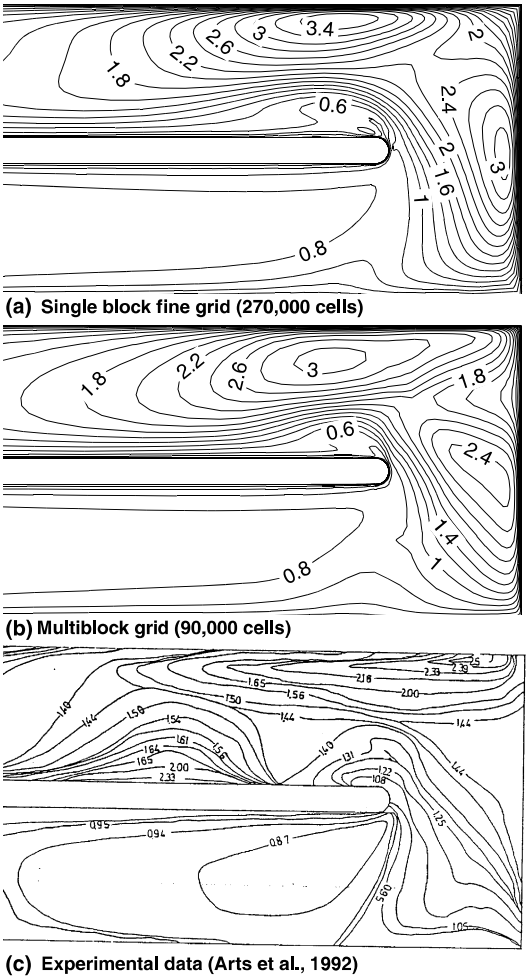

Fig. 35. Normalized Nusselt number contours on the bottom wall for $Re = 17,000$ and aspect ratio of 0.5 (Rigby et al., 1996).

5.1. Ribs and bleed holes

Rigby et al. (1997a) simulated numerically the flow in a straight channel with square cross-section. While three of the walls of the channel were smooth, the remaining wall was simulated to possess a combination of ribs and bleed holes. Reynolds numbers from 10,000 to 38,000 based on the hydraulic diameter (D) were considered. The rib height as well as the hole diameter was taken to be $D/8$. Fig. 37 shows every other grid point in the symmetry plane for the wall with ribs and holes. Three multi-block grid systems were generated for the case with ribs and holes, the case with just ribs, and the case with just holes. The initial number of blocks for each case was 124, 96, and 94, which were merged to 20, 12, and 16, respectively, using the Method of Weakest Descent (Rigby, 1996; Rigby et al., 1997b). Fig. 38 shows the spanwise-averaged Nusselt number on the bottom wall, normalized by the value for a fully developed turbulent pipe flow, as a function of the downstream distance. The experimental data in Fig. 38 were provided by Ekkad et al. (1996). Results for the case with both ribs and bleed holes are shown in Fig. 38(a). The heat transfer is low just downstream of the rib, rises sharply as the region of reattachment is approached, and then drops somewhat near the upstream side of the rib. Also, a sharp rise in heat transfer is observed downstream of the bleed hole. Looking at the last pitch in Fig. 38(a), one can see that agreement with the experimental data is excellent in the region between the ribs. In the computed data, the first two pitches have developing flow, and thus are not expected to compare to the experimental data. On the rib tops, the computed results do show Nusselt number ratios as high as four near the centerline of the channel; however, the spanwise average falls significantly below the experimental data. Reasons for the under-prediction on the rib tops may be insufficient grid resolution locally or accuracy of the experimental data near a surface discontinuity. Figs. 38(b) and (c) show a similarly good agreement with the experimental data for just holes and just ribs, respectively. Fig. 38(d) shows the results for the smooth wall case. The rise in the experimental data in Fig. 38(d) represents data in the 180° turn which was not modeled by Rigby et al. (1997a).

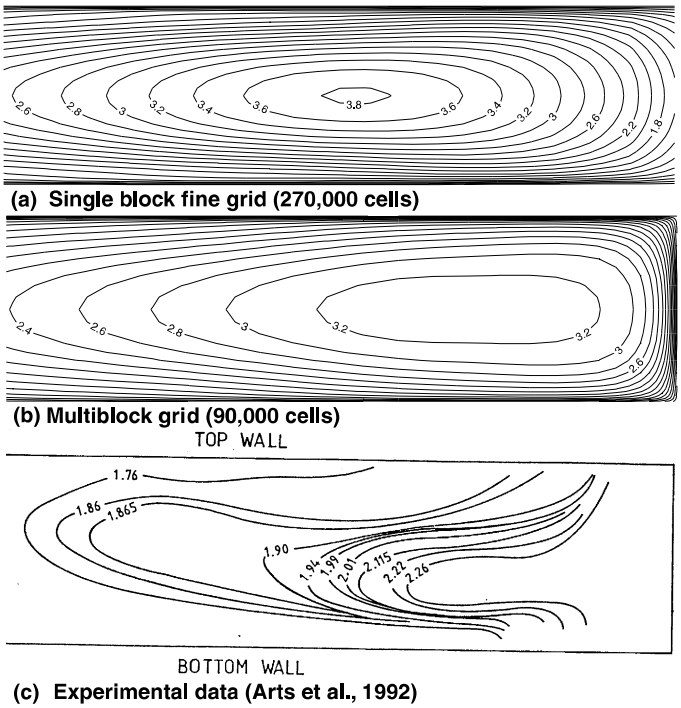

Fig. 36. Normalized Nusselt number contours on the side wall for $Re = 17,000$ and aspect ratio of 0.5 (Rigby et al., 1996).

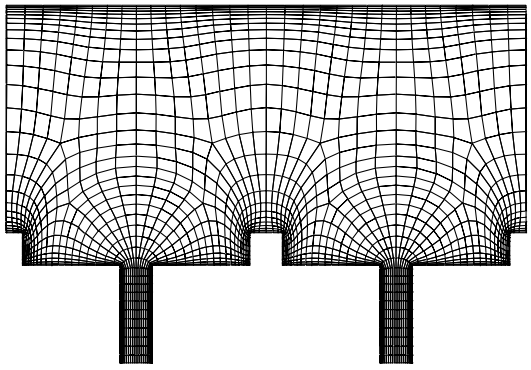

Fig. 37. Grid in the symmetry plane (Rigby et al., 1997a).

5.2. Rotating channel

Rigby (1998) presented numerical results for flow in a rotating passage with a 180° turn and ribbed walls. Reynolds numbers ranging from 5200 to 7900 (in order to match those for the experimental data), and rotation numbers of 0.0 and 0.24 were considered. The straight sections of the channel had a square cross-section, with square ribs spaced one hydraulic diameter (D) apart on two opposite sides, with a rib height of $0.1D$. For the low Reynolds numbers considered, the standard k–ω turbulence model did not produce reattachment between the ribs. By modifying the wall boundary condition on ω, much better agreement with the flow structure and heat/mass transfer was achieved. Fig. 39 shows the grid around the ribs. It also shows how viscous grids are not allowed to propagate into the inviscid region where they are not needed. The entire grid contained 1.49 million cells. Rigby (1998) presented mass transfer values in terms of the Sherwood number normalized by the empirical value for a fully developed turbulent pipe flow. Fig. 40 shows the mass transfer results for the rotating case rot36, corresponding to $Re = 5250$ and $Ro = 0.244$. The levels observed for this case are within the range observed in the experimental data of Park (1996). The patterns are also very similar to those of the experiment. Notice that, in general, the trailing surface in the first leg has higher values than the leading surface. The opposite is true in the second leg. High values are seen on both surfaces near the endwall and near the outside of the second turn. Also seen in the experimental data (Park, 1996) is the double peak in the first rib pitch in the second leg. Fig. 41 shows the spanwise-averaged Sherwood number in the first leg for the rotating case rot36 along with the data of Park (1996). The trailing wall results agree well with the data, especially in the latter half of the leg. The leading wall values are somewhat higher than the data. Fig. 42 shows the results in the second leg for the same case. The agreement with the experimental data is quite good for the trailing wall, especially in the downstream half. The leading wall, on the other hand, is generally under-predicted.

5.3. Experimental data

Thurman and Poinsatte (2001) provide experimental data for heat transfer in a simple 3-leg serpentine test section with ribs and bleed holes. Steady-state heat

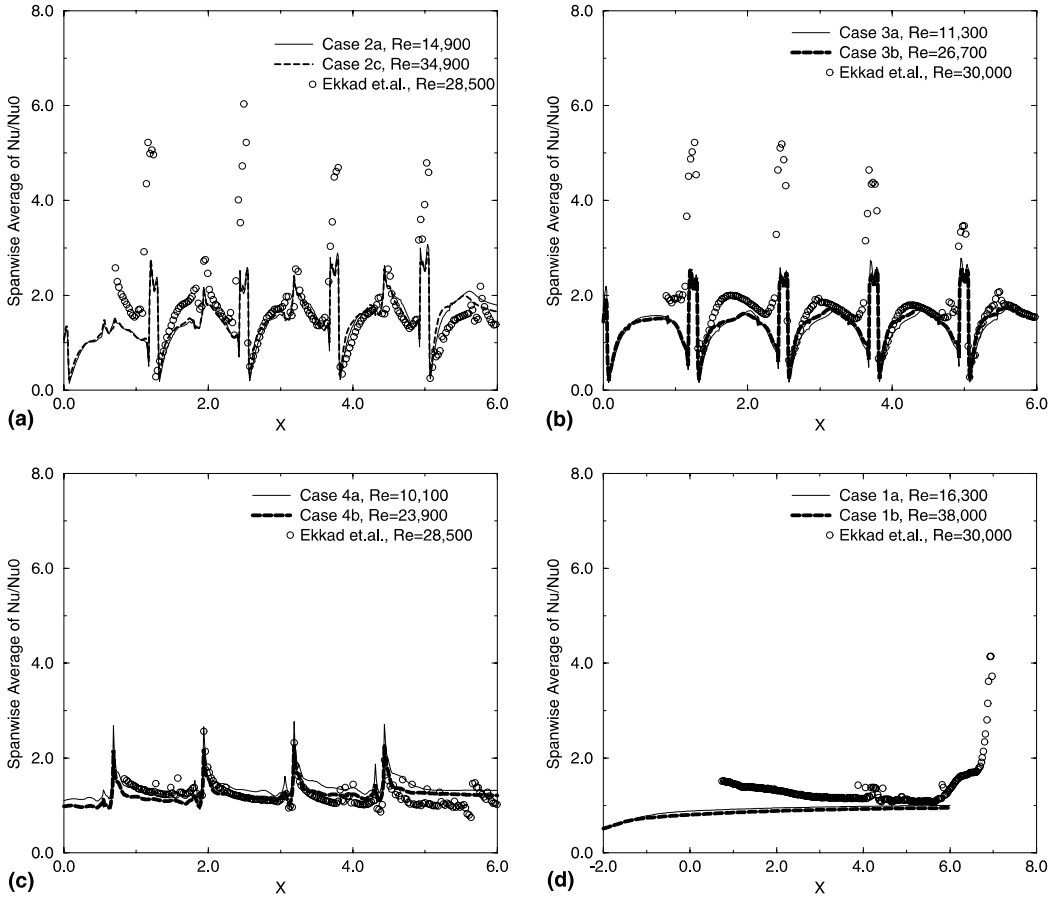

Fig. 38. Spanwise-averaged Nu/Nu_o (Rigby et al., 1997a). (a) Ribs and holes; (b) just ribs; (c) just holes; (d) smooth.

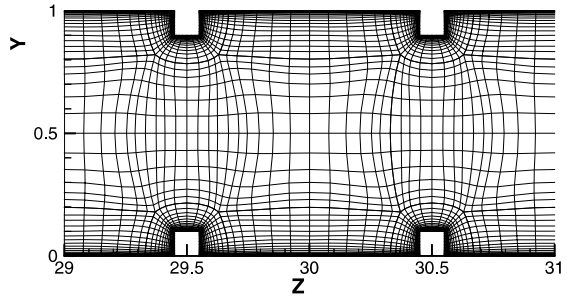

Fig. 39. Grid in the plane $x = 0$ (Rigby, 1998).

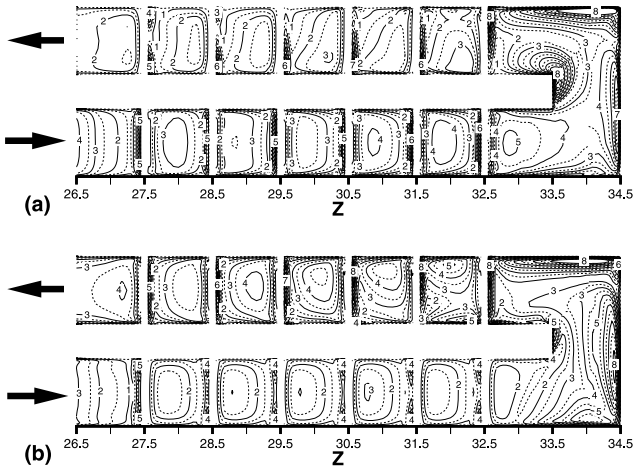

Fig. 40. Normalized Sherwood number for case rot36 (Rigby, 1998). (a) Trailing surface ($y = 1$); (b) leading surface ($y = 0$).

transfer measurements were obtained using a transient technique with thermochromic liquid crystals for Reynolds numbers of 31,000, 61,000 and 96,000. When bleed was employed, the bleed flow rates were nominally 10% of the inlet mass flow for the lowest Reynolds number, and 5% for the two higher Reynolds numbers. Trip strips were attached to one wall of the test section and were located either between or near the bleed holes. Heat transfer enhancement was found to be greater for ribs near bleed holes compared to ribs between holes, and both configurations were affected slightly by bleed rates upstream. Average bulk air temperatures, measured at discrete locations along one leg of the model, were found to remain fairly constant.

Thurman and Poinsatte (2001) presented heat transfer results as the ratio of Nusselt number for the flow to that for fully developed turbulent pipe flow. Fig. 43 shows the heat transfer distribution for ribs near the

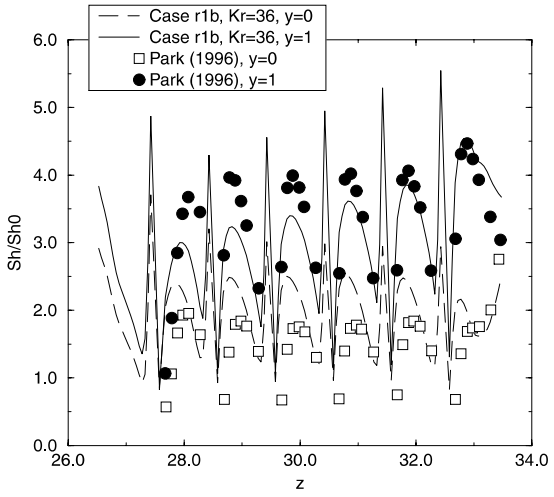

Fig. 41. Spanwise-averaged Sherwood number in the first leg for the case rot36 (Rigby, 1998).

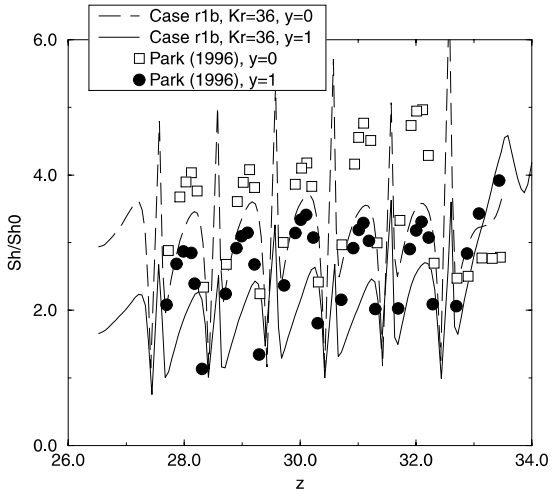

Fig. 42. Spanwise-averaged Sherwood number in the second leg for the case rot36 (Rigby, 1998).

bleed holes. Fig. 43(a) corresponding to the no bleed case shows no effect from the holes, as expected. Figs. 43(b)–(d) show that heat transfer is greatly enhanced near the downstream edge of the ribs due to the bleeding of the stagnant separated flow behind the rib. The patterns produced by bleed are C-shaped, opposite to those produced by the ribs-between-hole configuration. Other than the mirrored patterns, heat transfer trends for each case are similar to those for ribs between holes. For uniform bleed, Fig. 43(b), heat transfer distributions are periodic with higher Nusselt numbers near the bleed holes. Downstream of the hole, the effect of bleed is reduced near the upstream edge of the rib.

Heat transfer upstream for the increasing bleed case, Fig. 43(c), is similar to the no bleed case; heat transfer downstream is similar to the uniform bleed case, with slightly better enhancement away from the hole. Near holes 4 and 5, where bleed rates are about the same as those with uniform bleed, normalized Nusselt number values away from the hole are similar to those for uniform bleed and higher near the hole. With decreasing bleed, Fig. 43(d), heat transfer upstream is similar to the uniform bleed case, with higher values near and away from the hole. Heat transfer downstream is better than that without bleed but not as good as with uniform bleed. Near holes 4 and 5, heat transfer is similar to uniform bleed away from the hole, but is higher near the hole. By comparing the distributions near holes 4 and 5, it appears that the decreasing bleed case gives better heat transfer enhancement.

6. Rough blade heat transfer

The new (smooth) blade becomes rough with use in the engine. It is therefore important to understand the effects of surface roughness on turbine blade heat transfer. The surface roughness is expected to increase the blade surface heat transfer. If the surface roughness results from the deposition of low thermal conductivity material on the blade surface, the heat load, and therefore blade temperature, may decrease due to higher thermal resistance of the deposition layer. However, if surface roughness results from material erosion, understanding blade heat transfer becomes more critical, since blade strength decreases, and average blade temperature increases due to higher gas side heat transfer. Boyle et al. (2000, 2001) describe the recent experimental and computational work in this field. They used an infrared camera in order to make non-contact surface temperature measurements. Tests were conducted in a three-vane linear cascade, with inlet pressures between 14 and 103 kPa, exit Mach numbers of 0.3, 0.7 and 0.9, and for turbulence intensities of approximately 1% and 13%. Data from six profilometer traces were used to determine the roughness characteristics of the heated surface. For the rough vane, the heat transfer coefficient on the rear part of the suction surface was greater than that expected for a smooth vane by nearly a factor of 2 at high Reynolds numbers.

Fig. 44 shows stagnation point heat transfer in terms of Frossling number, Fr, for the turbulence grid with more than 13% turbulence intensity measured one axial chord upstream of the leading edge. The trend of an increasing Frossling number with increase in Reynolds number is similar to the no grid data, but the slope, especially in the lower Reynolds number region, is greater. This figure also shows the prediction using a correlation developed by Van Fossen et al. (1995) for a smooth leading edge. Primarily because of the large turbulent length scale to leading edge diameter ratio, the correlation gives a relatively small increase in Frossling number. Over much of the Reynolds number range, the

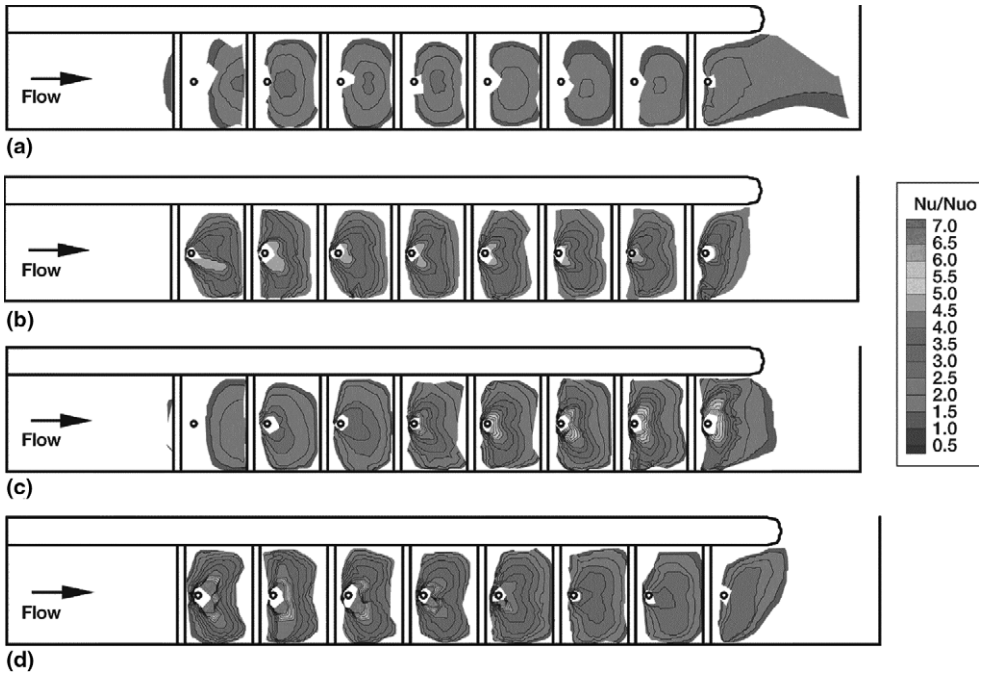

Fig. 43. Surface heat transfer, Nu/Nu_o, for the case of ribs near holes for $Re = 31,000$. (a) No bleed; (b) uniform bleed; (c) increasing bleed; (d) decreasing bleed (Thurman and Poinsatte, 2001).

effect of roughness on Frossling number is significantly greater.

The degree to which surface roughness affects the flow and heat transfer was determined by its value in wall normalized coordinates. The maximum normalized roughness height, h^+_{EQ}, was estimated using the procedure proposed by Boyle and Giel (1995) to estimate the maximum near wall grid spacing prior to a CFD calculation. Fig. 45 shows h^+_{EQ} as a function of the exit Reynolds number, Re_2, and h_{EQ}/C_x for two friction factors. The curves labeled SMOOTH are for a C_f ratio of 1, while those labeled ROUGH are for fully rough flow using the relationship given by Kays and Crawford (1980) for C_f. This figure shows that h^+_{EQ} increases almost linearly with Reynolds number and with the roughness height. For $h^+_{EQ} > 70$, the ROUGH curve is the appropriate curve to use for estimating h^+_{EQ}. For $5 < h^+_{EQ} < 70$, the appropriate value for h^+_{EQ} lies between the two curves. Fortunately, in this region the differences between the SMOOTH and ROUGH curves are small.

Fig. 46 shows the Nusselt number distribution over the entire span, after correcting for the non-uniformity in the electrical heat flux, for $Re_2 = 0.394 \times 10^6$,

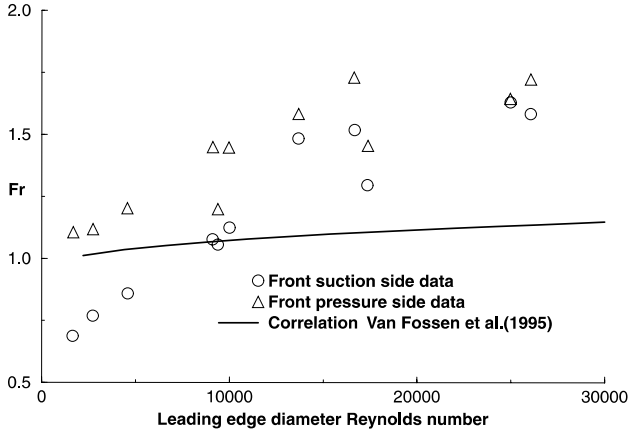

Fig. 44. Frossling number at vane stagnation point with turbulence grid (Boyle et al., 2001).

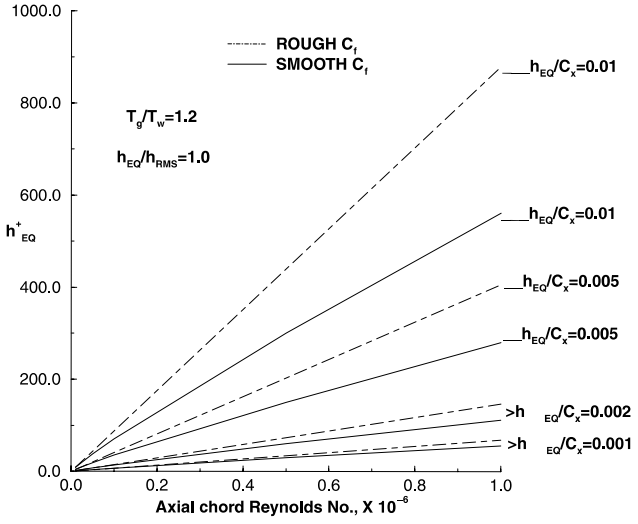

Fig. 45. Estimated maximum equivalent roughness height (Boyle et al., 2001).

$M_2 = 0.7$, and with turbulence grid. The pressure side view shows a low Nusselt number region on the pressure side of the leading edge. The heat transfer increases towards the leading edge and beyond. The suction front view shows high heat transfer on the pressure side, a decrease in heat transfer, followed by an increase on the suction side of the vane. The suction rear view shows a fairly uniform level over much of the region away from the end bus bars. Midway along the surface of this view, and near mid-span, there is a high heat transfer region. Either high surface roughness or over-estimating heat generation in this region could account for this high heat transfer.

Fig. 47 shows the Stanton number at $s/C_x = 2.5$. This location was chosen because the heat transfer coefficient is representative of the rear part of the suction surface. In addition to the experimental data, correlation for a smooth surface is shown along with results from a correlation given by Kays and Crawford (1980) for rough surfaces. For the no grid, lowest Reynolds number case, Stanton number is below the turbulent correlation, and is consistent with that for laminar flow. The data for the next highest Reynolds number are close to the smooth correlation for turbulent flow. At this and lower Reynolds numbers, the flow appears to be hydraulically smooth, as it does also for the grid cases. The no grid cases show a rapid increase, followed by a decrease, in Stanton number, eventually approaching the $h_{EQ}/C_x = 0.005$ curve at high Reynolds numbers. Stanton numbers just after transition are typically higher than the turbulent value. The expected value for h_{EQ}/C_x was 0.005. With the turbulence grid in place, the trend shows higher Stanton numbers at lower Reynolds numbers, and a more negative slope of Stanton number versus Reynolds number. The grid Stanton numbers approach the no grid values at high Reynolds numbers.

Boyle et al. (2000) compared the two-dimensional Navier–Stokes heat transfer predictions with their experimental data on the rough vane. Most of these comparisons are not shown here for the sake of brevity. The salient conclusions resulting from these comparisons are, however, described. Predictions were obtained using the code RVCQ3D (Chima, 1987), and employing both algebraic and k–ω turbulence models. The algebraic model incorporated the Cebeci–Chang roughness model (Cebeci and Chang, 1978). The k–ω model (Chima, 1996) accounts for roughness in the boundary condition. The k–ω results agreed better with the experimental data than the Cebeci–Chang model. The low Reynolds number k–ω model, L$k\omega$, did not accurately account for roughness at low freestream turbulence levels. The high Reynolds number version of this model, H$k\omega$, was more suitable at low turbulence levels. The H$k\omega$ formulation gave early transition at moderate Reynolds numbers and low turbulence intensities. This was consistent with the experimental data. The L$k\omega$ formulation showed transition like behavior at low turbulence intensities, which was inconsistent with the data. Also, for rough surface heat transfer prediction, an accurate knowledge of the equivalent roughness height is essential. Reducing the variation among various correlations for the equivalent height is as important as improving the turbulence model for rough surface heat transfer predictions.

Fig. 48 shows comparison with data for the H$k\omega$ model for $M_2 = 0.7$ and no turbulence grid. The agreement is satisfactory both in the leading edge region and over the rear of the suction surface. The data illustrate

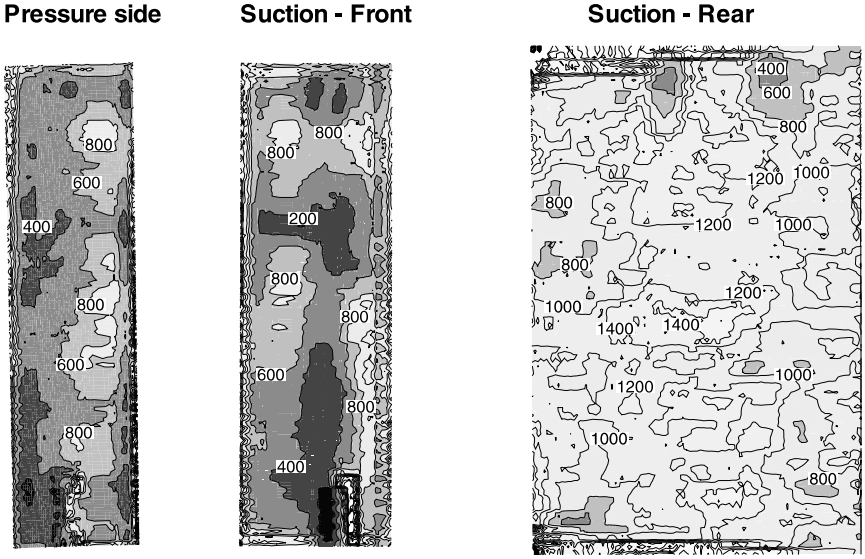

Fig. 46. Nusselt number contours for $Re_2 = 0.394 \times 10^6$, $M_2 = 0.7$ and non-uniform heat flux (Boyle et al., 2001).

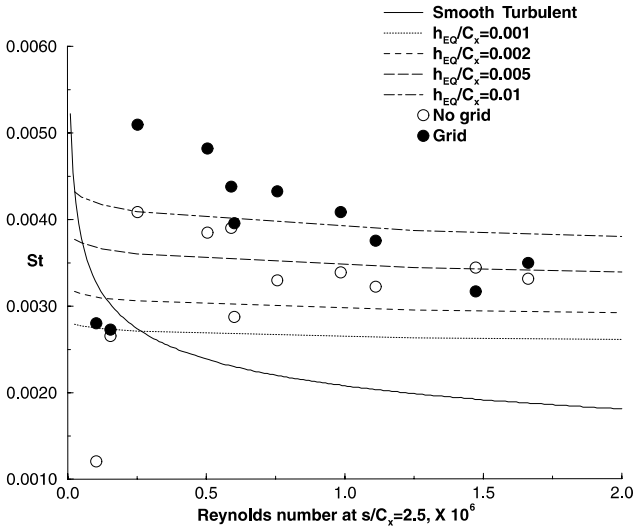

Fig. 47. Stanton number at $s/C_x = 2.5$ (Boyle et al., 2001).

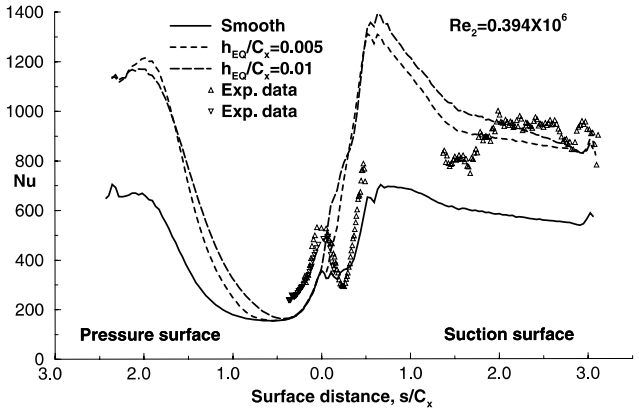

Fig. 48. Nusselt number comparisons for $M_2 = 0.7$, no turbulence grid and H$k\omega$ model (Boyle et al., 2000).

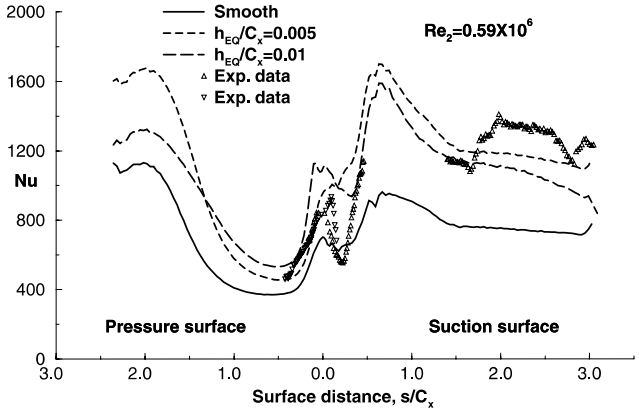

Fig. 49. Nusselt number comparisons for $M_2 = 0.7$, with turbulence grid and H$k\omega$ model (Boyle et al., 2000).

that continually increasing the roughness height results in only small changes in the predicted heat transfer. Fig. 48 shows a similar comparison of H$k\omega$ results with the data for the turbulence grid case. Again, the agreement is reasonable. The results shown in Fig. 49 illustrate a difficulty observed with the H$k\omega$ model. The predictions show a maximum Nusselt number at an intermediate roughness height. This was surprising and the cause for this was found to be the sensitivity of the H$k\omega$ model to the near-wall grid line spacing. Many more comparisons are available in Boyle et al. (2000).

7. Concluding remarks and future directions

In this presentation we have attempted to describe the research related to heat transfer in gas turbines being conducted at the NASA Glenn Research Center. This research supports a broad spectrum of government and industry needs that are principally manifested in focused program activities. In addition, it is part of the NASA Base R&T program with a longer-term focus. While much has been achieved, more needs to be done in terms of validating the predictions against experimental data. More experimental data, especially on film-cooled and rough turbine blades, are required for code validation. Also, the combined film cooling and internal cooling flow computation for a real blade is yet to be performed. While most computational work to date has assumed steady-state conditions, the flow is clearly unsteady due to the presence of wakes. Computation of heat transfer under unsteady conditions is still very expensive and time consuming. In order to impact the design time and cost, however, the turbine blade designer should be able to evaluate different designs quickly. All this points to a long road ahead!

Acknowledgements

The author wishes to thank Dr. Raymond Gaugler, Chief, Turbine Branch at the NASA Glenn Research Center for his support of this work. Help from my colleagues namely, Ali Ameri, Robert Boyle, Jim Heidmann, David Rigby and Douglas Thurman, is also greatly appreciated.

References

Ameri, A.A., Arnone, A., 1996. Transition modeling effects on turbine rotor blade heat transfer predictions. J. Turbomachinery 118, 307–313.

Ameri, A.A., Bunker, R.S., 2000. Heat transfer and flow on the first-stage blade tip of a power generation gas turbine: part 2 – simulation results. J. Turbomachinery 122, 272–277.

Ameri, A.A., Rigby, D.L., 1999. A numerical analysis of heat transfer and effectiveness on film cooled turbine blade tip models. NASA CR 1999-209165. Also Proc. 14th Internat. Symp. Air Breathing Engines (ISABE), Florence, Italy.

Ameri, A.A., Steinthorsson, E., 1995. Prediction of unshrouded rotor blade tip heat transfer. ASME Paper 95-GT-142.

Ameri, A.A., Steinthorsson, E., 1996. Analysis of gas turbine rotor blade tip and shroud heat transfer. ASME Paper 96-GT-189.

Ameri, A.A., Steinthorsson, E., Rigby, D.L., 1998. Effect of squealer tip on rotor heat transfer and efficiency. J. Turbomachinery 120, 753–759.

Ameri, A.A., Steinthorsson, E., Rigby, D.L., 1999. Effects of tip clearance and casing recess on heat transfer and stage efficiency in axial turbines. J. Turbomachinery 121, 683–693.

Arnone, A., 1992. Notes on the use of the JERRY and TOM grid generation codes, unpublished.

Arnone, A., 1994. Viscous analysis of three-dimensional rotor flow using a multigrid method. J. Turbomachinery 116, 435–445.

Arnone, A., Liou, M.-S, Povinelli, L.A., 1991. Multigrid calculation of three-dimensional viscous cascade flows. AIAA Paper 91-3238.

Arnone, A., Liou, M.-S, Povinelli, L.A., 1992. Navier–Stokes solution of transonic cascade flow using non-periodic C-type grids. AIAA J. Propul. Power 8, 410–417.

Arts, T., Lambert de Rouvroit, M., Rau, G., Acton, P., 1992. Aero-thermal investigation of the flow developing in a 180 degree turn channel. VKI pre-print No. 1992-10.

Blair, M.F., 1991. The effects of Reynolds number, rotor incidence angle, and surface roughness on the heat transfer distribution in a large scale turbine rotor. UTRC Report R91-970057-3.

Boyle, R.J., 1991. Navier–Stokes analysis of turbine blade heat transfer. J. Turbomachinery 113, 392–403.

Boyle, R.J, Ameri, A.A., 1997. Grid orthogonality effects on predicted turbine midspan heat transfer and performance. J. Turbomachinery 119, 31–38.

Boyle, R.J., Giel, P., 1995. Three-dimensional Navier–Stokes heat transfer predictions for turbine blade rows. AIAA J. Propul. Power 11, 1179–1186.

Boyle, R.J., Giel, P.W., 2001. Prediction of relaminarization effects on turbine blade heat transfer. ASME Paper 2001-GT-162.

Boyle, R.J., Jackson, R., 1997. Heat transfer predictions for two turbine nozzle geometries at high Reynolds and Mach numbers. J. Turbomachinery 119, 270–283.

Boyle, R.J., Russell, L.M., 1990. Experimental determination of stator endwall heat transfer. J. Turbomachinery 112, 547–558.

Boyle, R.J., Simon, F.F., 1998. Mach number effects on turbine blade transition length prediction. ASME Paper 98-GT-367.

Boyle, R.J., Spuckler, C.M., Lucci, B.L., 2000. Comparison of predicted and measured turbine vane rough surface heat transfer. ASME Paper 2000-GT-217.

Boyle, R.J., Spuckler, C.M., Lucci, B.L., Camperchioli, W.P., 2001. Infrared low-temperature turbine vane rough surface heat transfer measurements. J. Turbomachinery 123, 168–177.

Bunker, R.S., Bailey, J.C., Ameri, A.A., 2000. Heat transfer and flow on the first-stage blade tip of a power generation gas turbine: part 1 – experimental results. J. Turbomachinery 122, 263–271.

Camci, C., Arts, T., 1985. Experimental heat transfer investigation around the film-cooled leading edge of a high-pressure gas turbine rotor blade. J. Eng. Gas Turbines Power 107, 1016–1021.

Cebeci, T., Chang, K.C., 1978. Calculation of incompressible rough wall boundary-layer flows. AIAA J. 16, 730–735.

Chima, R.V., 1987. Explicit multigrid algorithm for quasi-three-dimensional flows in turbomachinery. AIAA J. Propul. Power 3, 397–405.

Chima, R.V., 1991. Viscous three-dimensional calculations of transonic fan performance. In: AGARD Propulsion and Energetics Symposium on Computational Fluid Mechanics for Propulsion, San Antonio, TX, May 27–31.

Chima, R.V., 1996. A k–ω turbulence model for quasi-three-dimensional turbomachinery flows. AIAA Paper 96-0248.

Chima, R.V., Giel, P.W., Boyle, R.J., 1993. An algebraic turbulence model for three-dimensional viscous flows. AIAA Paper 93-0083. Also NASA TM-105931.

Chima, R.V., Yokota, J.W., 1990. Numerical analysis of three-dimensional viscous internal flows. AIAA J. 28, 798–806.

Dunn, M.G., Kim, J., Civinskas, K.C., Boyle, R.J., 1994. Time-averaged heat transfer and pressure measurements and comparison with prediction for a two-stage turbine. J. Turbomachinery 116, 14–22.

Ekkad, S.V., Huang, Y., Han, J.C., 1996. Detailed heat transfer distributions in two-pass smooth and turbulated square channels with bleed holes. In: National Heat Transfer Conference, Houston, TX, vol. 8, pp. 133–140.

Garg, V.K., 1997. Adiabatic effectiveness and heat transfer coefficient on a film-cooled rotating blade. Numer. Heat Transfer, Part A 32, 811–830.

Garg, V.K. (Ed.), 1998a. Applied Computational Fluid Dynamics. Marcel Dekker, New York (Chapter 4).

Garg, V.K., 1998b. Heat transfer on a film-cooled rotating blade using a two-equation turbulence model. Int. J. Rotating Machinery 4 (3), 201–216.

Garg, V.K., 1999. Heat transfer on a film-cooled rotating blade using different turbulence models. Int. J. Heat Mass Transfer 42, 789–802.

Garg, V.K., 2000. Heat transfer on a film-cooled rotating blade. Int. J. Heat Fluid Flow 21, 134–145.

Garg, V.K., 2001. Modeling film-coolant flow characteristics at the exit of shower-head holes. Int. J. Heat Fluid Flow 22, 134–142.

Garg, V.K., Abhari, R.S., 1997. Comparison of predicted and experimental Nusselt number for a film-cooled rotating blade. Int. J. Heat Fluid Flow 18, 452–460.

Garg, V.K., Ameri, A.A., 1997. Comparison of two-equation turbulence models for prediction of heat transfer on film-cooled turbine blades. Numer. Heat Transfer, Part A 32, 347–371.

Garg, V.K., Ameri, A.A., 2001. Two-equation turbulence models for prediction of heat transfer on a transonic turbine blade. Int. J. Heat Fluid Flow 22, 593–602.

Garg, V.K., Gaugler, R.E., 1993. Heat transfer in film-cooled turbine blades. ASME Paper 93-GT-81.

Garg, V.K., Gaugler, R.E., 1994. Prediction of film cooling on gas turbine airfoils. ASME Paper 94-GT-16.

Garg, V.K., Gaugler, R.E., 1996. Leading edge film cooling effects on turbine blade heat transfer. Numer. Heat Transfer, Part A 30, 165–187.

Garg, V.K., Gaugler, R.E., 1997a. Effect of velocity and temperature distribution at the hole exit on film cooling of turbine blades. J. Turbomachinery 119, 343–351.

Garg, V.K., Gaugler, R.E., 1997b. Effect of coolant temperature and mass flow on film cooling of turbine blades. Int. J. Heat Mass Transfer 40, 435–445.

Garg, V.K., Rigby, D.L., 1999. Heat transfer on a film-cooled blade – effect of hole Physics. Int. J. Heat Fluid Flow 20, 10–25.

Giel, P.W., Thurman, D.R., Van Fossen, G.J., Hippensteele, S.A., Boyle, R.J., 1998. Endwall heat transfer measurements in a transonic turbine cascade. J. Turbomachinery 120, 305–313.

Giel, P.W., Van Fossen, G.J., Boyle, R.J., Thurman, D.R., Civinskas, K.C., 1999. Blade heat transfer measurements and predictions in a transonic turbine cascade. ASME Paper 99-GT-125.

Goldstein, R.J., 1971. Film cooling. Adv. Heat Transfer 7, 321–379.

Heidmann, J.D., Hunter, S.D., 2001. Coarse grid modeling of turbine film cooling flows using volumetric source terms. ASME Paper 2001-GT-138.

Heidmann, J.D., Rigby, D.L., Ameri, A.A., 2000. A three-dimensional coupled internal/external simulation of a film-cooled turbine vane. J. Turbomachinery 122, 348–359.

Hylton, L.D., Nirmalan, V., Sultanian, B.K., Kaufman, R.M., 1988. The effects of leading edge and downstream film cooling on turbine vane heat transfer. NASA CR 182133.

Jameson, A., Schmidt, W., Turkel, E., 1981. Numerical solutions of the Euler equations by finite volume methods using Runge–Kutta time-stepping schemes. AIAA Paper 81-1259.

Jones, W.P., Launder, B.E., 1973. The calculation of low-Reynolds-number phenomena with a two equation model of turbulence. Int. J. Heat Mass Transfer 16, 1119–1130.

Kays, W.M., Crawford, M.E., 1980. In: Convective Heat and Mass Transfer, second ed. McGraw-Hill, New York, p. 327.

Kim, Y.W., Metzger, D.E., 1995. Heat transfer and effectiveness on film cooled turbine blade tip models. J. Turbomachinery 117, 12–21.

Leylek, J.H., Zerkle, R.D., 1994. Discrete-jet film cooling: a comparison of computational results with experiments. J. Turbomachinery 116, 358–368.

Mayle, R.E., 1991. The role of laminar-turbulent transition in gas turbine engines. J. Turbomachinery 113, 509–537.

Menter, F.R., 1993. Zonal two-equation k–ω turbulence models for aerodynamic flows. AIAA Paper 93-2906.

Menter, F.R., 1994. Two-equation eddy–viscosity turbulence models for engineering applications. AIAA J. 32, 1598–1605.

Park, C.W., 1996. Local heat/mass transfer distributions in rotating two-pass square channels. Ph.D. Dissertation, Department of Mechanical Engineering, Texas A&M University, College Station, TX.

Program Development Corporation, 1997. GridPro™/az3000 – User's Guide and Reference Manual, White Plains, NY.

Rigby, D.L., 1996. Method of weakest descent for automatic block merging. In: Proc. 15th Internat. Conf. on Numer. Methods in Fluid Dynamics, Monterey, CA.

Rigby, D.L., 1998. Prediction of heat and mass transfer in a rotating ribbed coolant passage with a 180 degree turn. ASME Paper 98-GT-329.

Rigby, D.L., Ameri, A.A., Steinthorsson, E., 1996. Internal passage heat transfer prediction using multiblock grids and a k–ω turbulence model. ASME Paper 96-GT-188.

Rigby, D.L., Steinthorsson, E., Ameri, A.A., 1997a. Numerical prediction of heat transfer in a channel with ribs and bleed. ASME Paper 97-GT-431.

Rigby, D.L., Steinthorsson, E., Coirier, W.J., 1997b. Automatic block merging using the method of weakest descent. AIAA Paper 97-0197.

Simoneau, R.J., Simon, F.F., 1993. Progress towards understanding and predicting heat transfer in the turbine gas path. Int. J. Heat Fluid Flow 14, 106–128.

Sorenson, R.L., 1980. A computer program to generate two-dimensional grids about airfoils and other shapes by the use of Poisson's equations. NASA TM 81198.

Steinthorsson, E., Ameri, A.A., Rigby, D.L., 1997. TRAF3D. MB – A multi-block flow solver for turbomachinery flows. AIAA Paper 97-0996.

Steinthorsson, E., Liou, M.S., Povinelli, L.A., 1993. Development of an explicit multiblock/multigrid flow solver for viscous flows in complex geometries. AIAA Paper 93-2380.

Thurman, D., Poinsatte, P., 2001. Experimental heat transfer and bulk air temperature measurements for a multipass internal cooling model with ribs and bleed. J. Turbomachinery 123, 90–96.

Van Fossen, G.J., Simoneau, R.J, Ching, C.Y., 1995. Influence of turbulence parameters, Reynolds number, and body shape on stagnation-region heat transfer. J. Heat Transfer 117, 597–603.

Wilcox, D.C., 1988. Reassessment of the scale-determining equation for advanced turbulence models. AIAA J. 26, 1299–1310.

Wilcox, D.C., 1994. Simulation of transition with a two-equation turbulence model. AIAA J. 32, 247–255.

Wilcox, D.C., 1998. Turbulence Modeling for CFD, second ed. DCW Industries.